Experimental sepsis-associated encephalopathy is accompanied by altered cerebral blood perfusion and water diffusion and related to changes in cyclooxygenase-2 expression and glial cell morphology but not to blood-brain barrier breakdown

Marion Griton, Ibtihel Dhaya, Renaud Nicolas, Gérard Raffard, Olivier Periot, Bassem Hiba, Jan Pieter Konsman

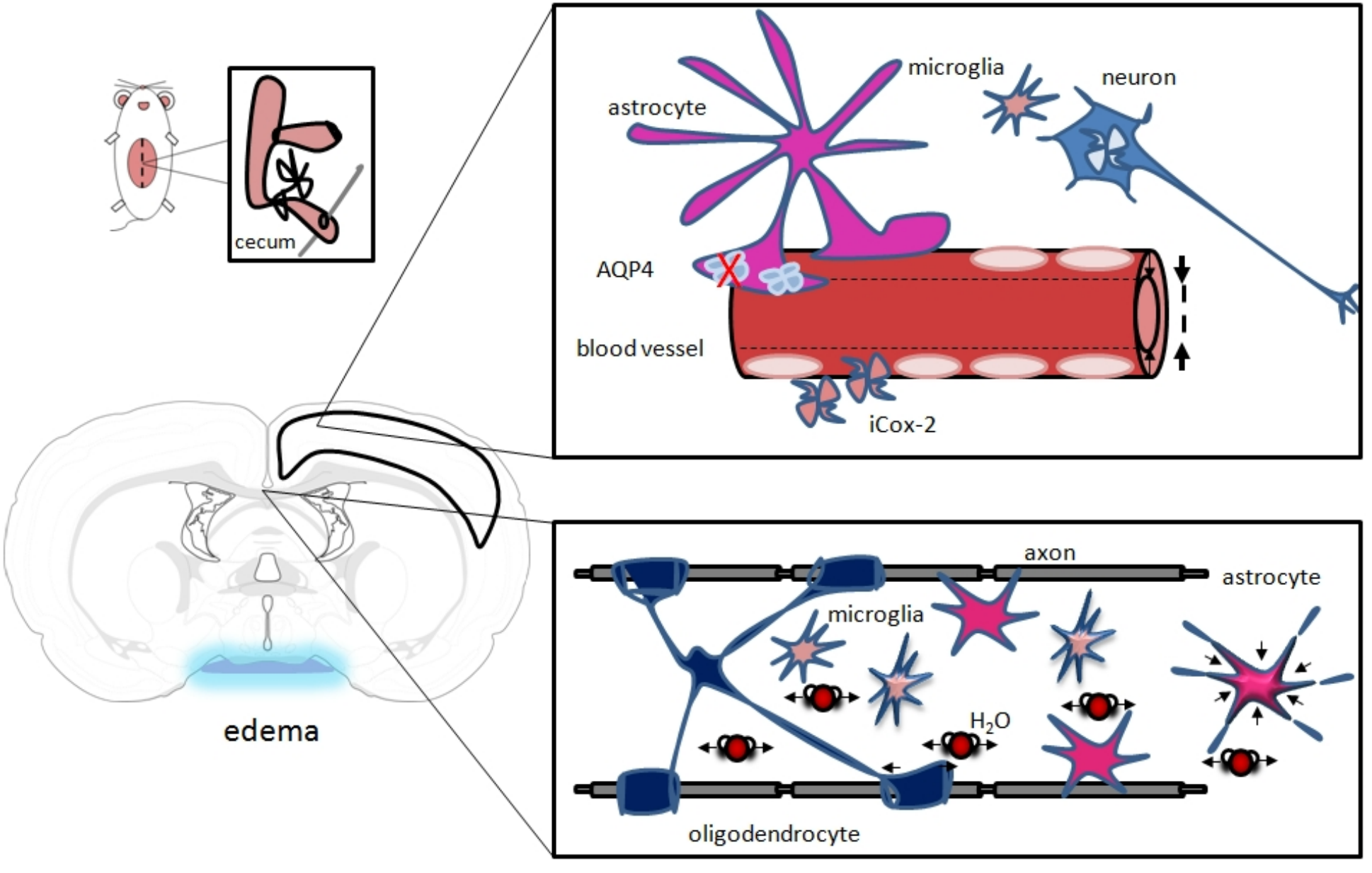
cecum
edema
astrocyte
microglia
neuron
AQP4
blood vessel
iCox-2
axon
astrocyte
microglia
H_2O
oligodendrocyte

Experimental sepsis-associated encephalopathy is accompanied by altered cerebral blood perfusion and water diffusion and related to changes in cyclooxygenase-2 expression and glial cell morphology but not to blood-brain barrier breakdown

Marion Griton[a,b,c$] ,Ibtihel Dhaya[a,b,d$], Renaud Nicolas[a,b], Gérard Raffard[e,f], Olivier Periot[a,b,g], Bassem Hiba[a,b,h#] and Jan Pieter Konsman[a,b#*]

a INCIA, Institut de Neurosciences Cognitive et Intégrative d'Aquitaine, UMR 5287, Bordeaux, France

b Univ. Bordeaux, INCIA, UMR 5287, Bordeaux, France

c Service de Réanimation Anesthésie Neurochirurgicale, Centre Hospitalier Universitaire (CHU) de Bordeaux, Bordeaux, France

d Laboratoire de Neurophysiologie Fonctionnelle et Pathologies, UR/11ES09, Faculté des Sciences Mathématiques, Physiques et Naturelles, Université de Tunis El Manar, Tunis, Tunisia

e CNRS, Résonance Magnétique des Systèmes Biologiques, UMR 5536, Bordeaux, France

f Univ. Bordeaux, RMSB, UMR 5536, Bordeaux, France

g Service de Médecine Nucléaire, Centre Hospitalier Universitaire (CHU) de Bordeaux, Bordeaux, France

h CNRS UMR 5229, Centre de Neurosciences Cognitives Marc Jeannerod, Bron, France

Running title: CLP increases white matter axial diffusion

$ contributed equally to the present work; # co-senior authors

* Corresponding author:
Aquitaine Institute for Integrative and Cognitive Neuroscience (INCIA) UMR CNRS 5287,
University of Bordeaux, 146 rue Léo Saignat, 33076 Bordeaux, France
Phone / Fax: (33) 5 57 57 15 51 / (33) 5 56 90 14 21
Email: jan-pieter.konsman@u-bordeaux.fr

Abstract

Sepsis-associated encephalopathy (SAE) refers to brain dysfunction, including *delirium*, occurs during severe infection and is associated with development of post-traumatic stress disorder. SAE has been proposed to be related to reduced cerebral blood flow (CBF), blood-brain barrier breakdown (BBB), white matter edema and disruption and glia cell activation, but their exact relationships remain to be determined. In the present work, we set out to study CBF using Arterial Spin Labeling (ASL) and grey and white matter structure with T2- and diffusion magnetic resonance imaging (dMRI) in rats with cecal ligation and puncture (CLP)-induced encephalopathy. Using immunohistochemistry, the distribution of the vasoactive prostaglandin-synthesizing enzyme cyclooxygenase-2 (COX-2), perivascular immunoglobulins G (IgG), aquaporin-4 (AQP4) and the morphology of glial cell were subsequently assessed in brains of the same animals. CLP induced deficits in the righting reflex and resulted in higher T2-weighted contrast intensities in the cortex, striatum and at the base of the brain, decreased blood perfusion distribution to the cortex and increased water diffusion parallel to the fibers of the corpus callosum compared to sham surgery. In addition, CLP reduced staining for microglia- and astrocytic-specific proteins in the corpus callosum, decreased neuronal COX-2 and AQP4 expression in the cortex while inducing perivascular COX-2 expression, but did not induce widespread perivascular IgG diffusion. In conclusion, our findings indicate that experimental SAE can occur in the absence of BBB breakdown and is accompanied by increased water diffusion anisotropy and altered glia cell morphology in brain white matter.

Introduction

Sepsis-associated encephalopathy (SAE) refers to brain dysfunction ranging from mild *delirium* to deep coma that occurs in up to 70% of patients with severe systemic infection (Gofton and Young, 2012; Jones and Griffiths, 2013; Lamar et al., 2011; Young, 2013). In addition to acute mental dysregulation in the form of *delirium*, sepsis also has long-term detrimental effects on mental health. Indeed, clinical sepsis is associated with the development of post-traumatic stress disorders (PTSD) months later (Boer et al., 2008; Rosendahl et al., 2013; Schelling et al., 2001; Wintermann et al., 2015).

In spite of its impact on mental and cognitive health, the mechanisms underlying SAE are poorly understood (Chaudhry and Duggal, 2014). SAE, including *delirium*, has been proposed to be related to reduced cerebral blood flow (CBF) and oxygen extraction, blood-brain barrier breakdown (BBB), brain inflammation and edema (Chaudhry and Duggal, 2014; Papadopoulos et al., 2000; Tsuruta and Oda, 2016). Indeed, baseline CBF has been shown to be reduced during SAE (Bowton et al., 1989; Maekawa et al., 1991; Pfister et al., 2008; Pierrakos et al., 2013; Pierrakos et al., 2014; Smith et al., 1998; Yokota et al., 2003). Furthermore, systematic assessment of middle cerebral artery (MCA) blood velocity to variations in arterial blood pressure indicates that impaired cerebral autoregulation is associated with sepsis-associated *delirium* (Pfister et al., 2008; Schramm et al., 2012). Of note, some authors have also suggested that loss of cerebral autoregulation sepsis-associated contributes to edema during sepsis (Piazza et al., 2009).

Interestingly, and concomitantly with vasospasms in the MCA of patients with sepsis and brain dysfunction, T2- and diffusion-weighted Magnetic Resonance Imaging (MRI) have indicated white matter vasogenic edema (Bartynski et al., 2006; Sharshar et al., 2007). Moreover, in patients who died of sepsis, dilation of the perivascular space accompanied by dissociation of myelinated and white matter microglial activation have been observed

(Lemstra et al., 2007; Sharshar et al., 2007; Zrzavy et al., 2019). Finally, *delirium* has been found to be associated with disruption of white matter organization at hospital discharge and 3 months later, which, in turn, was associated with long-term cognitive impairment (Morandi et al., 2012). So among the proposed underlying mechanisms, clinical SAE has been shown to be associated with reduced CBF, signs of edema formation and white matter changes. However, the relationships between these phenomena and the occurrence and role of BBB breakdown as well as glial activation remain to be determined.

Experimental models allowing to systematically vary factors of interest have the potential to unravel the pathophysiological mechanisms underlying SAE. Intravenous administration of bacterial lipopolysaccharide (LPS) fragments in human volunteers is sufficient to reduce global CBF (Moller et al., 2002; Pollard et al., 1997). However, after systemic administration of LPS in animals, some studies have also observed rapidly decreased global or incoming CBF (Bryan and Emerson, 1977; Christenson et al., 1986; Ekstrom-Jodal et al., 1982; Tempel et al., 1986; Villega et al., 2017; Wyler et al., 1969; Wyler et al., 1972), whereas others studies have shown increased CBF in cortical MCA territories, but dose-dependent impaired autoregulation of CBF (Rosengarten et al., 2007; Rosengarten et al., 2008). And although peripheral LPS administration in rodents induces microglial activation in different brain structures (Hoogland et al., 2015), no study so far seems to have assessed white matter.

Cecal ligation and puncture (CLP) is a more clinically-relevant sepsis model than systemic LPS administration in that it involves live bacteria and mimics the different hemodynamic phases observed in clinical sepsis. Interestingly, during the first 24 h after CLP, CBF has been shown to be preserved (Hinkelbein et al., 2007) while increased T2-weighted contrast at the base of the brain suggested vasogenic edema and decreased apparent diffusion coefficient (ADC) indicated cytotoxic edema in the cortex and hippocampus (Bozza et al., 2010).

The aim of the present work was to establish temporal and spatial relationships between CNS

hemodynamic, metabolic and structural changes during experimental sepsis using imaging and histological approaches on brains of the same animals. We studied CBF and brain microstructure using Arterial Spin Labeling (ASL) and Diffusion-weighted Magnetic Resonance Imaging (dMRI), respectively, in animals with SAE 24h after CLP. In addition, we also detected the vasoactive prostaglandin-synthesizing enzyme cyclooxygenase-2 (COX-2), which is upregulated under inflammatory response, the presence of perivascular immunoglobulins G (IgG) as a measure of BBB integrity, and modifications of glia cell morphology in the brains of the same animals.

Materials and methods

Animals

Twenty-one male 3.5 month old Wistar rats (Charles River, l'Abresle, France) weighing 340.3 ± 3.6 g were used. Animals were treated according to European recommendations on animal research (European Council Directive of 24 November 1986 (86/609/EEC) and European Parliament and Council Directive of 22 September 2010 (2010/63/UE)), housed 2 per cage in a temperature-controlled room (22.0 ± 1.0°C) with lights on from 8 AM to 8 PM with free access to water and food. After arrival rats were left undisturbed for at least a week except for daily handling starting three days before surgery.

Surgery

On the day of surgery, animals were anesthetized with isoflurane (induction 3-5%; maintenance 1.5% in air). Once anesthetized, seventeen rats underwent polymicrobial intra-abdominal infection induced by CLP as previously described (Rittirsch et al., 2009; Wichterman et al., 1980). Briefly, after a 2-3-cm midline abdominal incision, the cecum was exposed in sterile saline on laboratory film (Parafilm, Neenah, WI, USA) and ligated with a 4-0 silk suture (Ethicon, Issy les Moulineaux, France) just below the ileocecal valve and subsequently punctured twice with a 22 G sterile needle. Next, a small drop of cecal contents was gently pushed out, before the cecum was gently placed back into the peritoneal cavity and the abdomen was sutured in two layers. At the end of the operation, animals received 5 ml of saline and analgesia (butrophanol, Torbugesic®; 2 mg/kg subcutaneously) and were placed in a clean individual cage. For the ten rats that were sham-operated rats, the same manipulations were performed except cecal ligation and puncture and saline injection. Thirty minutes after the end of surgery animals were awake and moving around.

Behavioral evaluation

To study non-specific sickness responses during sepsis, daily food and water intake and body weight were measured at several time points prior and posterior to surgery.

Delirium involves, according to the *Diagnostic and Statistical Manual of Mental Disorders*, disturbances of consciousness or awareness and in attention (Meagher et al., 2014), and is therefore hard to assess in animals. However, SAE is routinely monitored through assessment of reflexes, for example as part of the Glasgow coma scale (Ebersoldt et al., 2007), and can thus be easily and robustly implemented in animals. Following Kadoi & Goto (2004), sham and CLP -operated rats were tested at different time points before and after surgery for two simple non-postural (pinna and corneal reflexes) and one complex postural somatomotor reflex (righting reflex).

The pinna reflex was assessed by lightly touching the auditory meatus with a cotton stick tip and recording the occurrence and rapidity of ear retraction or head shake. The corneal reflex was tested by gently touching the cornea with a cotton stick tip and scoring the occurrence and rapidity of eye blinks. The righting reflex consisted of picking up the animal behind the forepaws and holding its trunk horizontally back upwards before putting the animal's back down and evaluating the time required to turn over to an upright position.

Magnetic Resonance Imaging (MRI) acquisition and image processing

Twenty-four hours after surgery, animals were anesthetized again with isoflurane (induction 3-5%, maintenance 1.5%) and introduced into a 7T horizontal-bore scanner (Advance III console, Bruker, Ettlingen, Germany) equipped with a magnetic field gradient system providing a maximum magnetic field gradient amplitude of 650 mT/m. A quadrature coil was used for radio-frequency emission and a 4-element phased-array surface coil for signal reception. Intracolonic temperature was constantly monitored and the animal was heated

when colonic temperature dropped below 35.5°C by warm water circulating in the bed used to position the rat inside MRI scanner. Respiration was assessed with a ventral pressure sensor and heart rate recorded using an MRI compatible electrode. After careful second-order shimming, T1-weighted MRI, T2-weighted MRI, Arterial Spin Labeling (ASL) and diffusion-weighted MRI (dMRI) images were acquired (see supplementary Materials and Methods for details of MRI acquisition sequences).

Analysis of T2-weighted images was performed using mipav (https://mipav.cit.nih.gov). In this study, relative T2-weighted intensities were compared to determine the presence rather than the quantity of edematic fluid (Abdel-Aty et al., 2005). Volumes Of Interest (VOIs) were defined in the brain and in the skull muscles and expressed as ratios. The VOI at the base of the brain was made up of 3 parts (right, left and center) to avoid blood vessels. The corresponding VOIs were summed together to cover the base of the rat brain (in bregma ~ -0.46mm). The other VOIs were cortex, striatum (right and left) and corpus callosum. Maximum and average intensities obtained in brain VOIs were then divided by those obtained in the skull muscle.

ASL data processing was performed using ParaVision software (Bruker, Ettlingen, Germany) unless otherwise indicated. Two (selective and global) T1 maps were computed using slice-selective and global FAIR data sets. Relative cerebral blood flow (rCBF) map was then computed pixel by pixel according to Kober et al. (2004). Blood T1 measured on rat blood at 7 T was set at 2070 ms (Dobre et al., 2007; Esparza-Coss et al., 2010). To analyze perfusion data, Regions Of Interest (ROIs) corresponding to the global brain, brain hemispheres, grey matter of the cortex and striatum as well as to the white matter of the corpus callosum and external capsule were traced manually on each individual's selective inversion 1100ms FAIR image using a rat brain atlas (Swanson, 1998) for guidance. These ROIs were then copied onto perfusion maps images (Fig. 1).

189 A quality control was first performed on raw dMRI data and diffusion tensor imaging (DTI)
190 maps. The *3dSkullStrip* command included in Analysis of Functional NeuroImages software
191 (AFNI) (https://afni.nimh.nih.gov) was used for image processing 1) to extract the brain from
192 surrounding tissues and 2) to create a mask. The twenty-one DW images and the B0 images
193 were corrected for eddy currents using *eddy* and fitted to the DTI model with *dtifit* (both part
194 of the FMRIB's Software Library (FSL) (http://www.fmrib.ox.ac.uk/fsl)).
195 The following diffusion-tensor maps were computed: 1) Eigenvalues (λ1, λ2 and λ3)
196 corresponding to water molecule diffusivities along the principal axes of the diffusion tensor,
197 2) Axial Diffusivity (AD=λ1) representing water diffusivity along the length of the white
198 matter fibers, 3) Radial Diffusivity (RD=(λ2+λ3)/2)) representing water diffusivity
199 perpendicular to the white matter fibers. 4) Mean Diffusivity (MD=(λ1+λ2+λ3)/3) of water
200 molecules, 5) Fractional Anisotropy (FA calculated following Alexander (2000)) indicating
201 the degree of anisotropy of water diffusivity and 6) residuals maps as a quality assessment
202 tool for DTI regression accuracy showing artefacts that are not always visible on above maps.
203 Additional maps were then calculated to describe the shape of diffusion including 7)
204 Coefficient of sphericity (Cs) corresponding to the roundness of tensor ellipsoid, 8)
205 Coefficient of planar anisotropy (Cp) measuring planarity, and 9) Coefficient of linear
206 anisotropy (Cl) that assesses the tendency of the tensor ellipsoid to have a cigar shape
207 (Alexander et al., 2000).
208 ROIs were positioned manually on the white matter of the corpus callosum and external
209 capsule and the grey matter of the cortex and striatum at two different rostrocaudal levels: 1)
210 bregma -0.51mm (Swanson, 1998) and 2) bregma -1.08mm (Swanson, 1998) because the
211 cytoarchitecture of these structures is known to vary along the rostrocaudal axis (Barazany et
212 al., 2009). On Color-coded FA maps showing white matter in different colors according to
213 fiber orientations, additional ROIs were placed on the cortex and on the external capsule,

after which the part of the external capsule where axons run horizontally and the part where axons are oriented vertically were analyzed.

To explore diffusion data in a non-hypothesis driven manner, a whole brain voxelwise statistical method adapted to the rat brain was performed using Tract-Based Spatial Statistics (TBSS) which is part of FSL (Smith et al., 2006). FA maps from each rat were co-registered to the DTI Rat Atlas for Postnatal Day 72 (DTI-RAPnD72) template (https://www.nitrc.org/projects/dti_rat_atlas/) using *fnirt* a nonlinear registration command adapted to take into account rat brain. After image registration, FA maps were averaged to produce a group mean FA image. A skeletonization algorithm was applied to the group mean FA image to define a group template of the lines of maximum FA, thought to correspond to centers of white matter tracts. FA values for each individual subject were then projected onto the group template skeleton by searching along perpendiculars from the skeleton to find local maxima. Non-FA maps (AD, RD, and MD) were skeletonized according to non-linear warps of the FA registrations described above.

Tissue processing and immunohistochemistry

At the end of MRI, rats were deeply anaesthetized by intraperitoneal injection of 60mg/kg of sodium pentobarbital. Bodies were rinsed from blood by intracardiac perfusion with 0.1 M phosphate-buffered saline (PBS; pH 7.4) and subsequently fixed by 300 ml of 4% paraformaldehyde in 0.1 M PBS. Brains were removed from the skull, post-fixed for 4 h in the same fixative, and then cryoprotected in 30% sucrose in 0.1 M phosphate buffer. Thirty-micrometer thick sections were cut on a cryostat (CM3050 S, Leica Microsystems, Nussloch, Germany) from the rostral limit of the optic chiasm to the caudal end of the central amygdala (Swanson, 1998) and collected in cold cryoprotectant solution (0.05 M PBS, 20 % glycerol, 30% ethylene glycol) and stored at -20°C until processing.

Immunohistochemistry was performed as previously described (Konsman and Blomqvist, 2005; Konsman et al., 2008; Konsman et al., 2004). Briefly, free-floating sections were washed four times in 0.1 M PBS (pH 7.4). Non-specific binding sites were blocked by a 45-minute incubation of sections in PBS containing 0.3% Triton X-100 and 2.0% normal serum or 1.0% BSA. The first antibody was then diluted (indicated below for every antiserum used) in the same buffer and added to the sections overnight at room temperature.

Commercially available antisera raised against COX-2 (goat anti-COX-2; M-19 sc-1747, lot# F2512, Santa Cruz Biotechnology, Heidelberg, Germany) diluted 1:750, the microglia-macrophage specific ionized calcium-binding adaptor molecule (Iba-1; rabbit anti-Iba-1; 019-19741, Wako Chemicals GmbH, Neuss, Germany) diluted 1:1000 and rat immunoglobulin G (IgG; biotinylated goat anti IgG, BA-9401, Vector Laboratories, Burlingame, CA, USA) diluted 1:2000, the astrocytic aquaporin-4 water channel (rabbit anti-AQP4, cat # AB2218, lot # 2506432, Millipore, Fontenay sous Bois, France) diluted 1:2000, the intermediate filament Glial fibrillary acidic protein GFAP (mouse anti-GFAP mAb, clone GA5, MAB360, Merck Millipore, Fontenay sous Bois, France) diluted 1:500, the myelin-associated enzyme 2',3'-Cyclic-nucleotide 3'-phosphodiesterase also known as CNPase (mouse anti-CNPase, Abcam, Paris, France) diluted 1:8000 were used.

After four rinses in PBS, sections were treated for 30 minutes with 0.3% (v/v) hydrogen peroxide to block endogenous peroxidases followed by four rinses in PBS. With the exception of those sections exposed to biotinylated rat IgG, sections were then incubated for 2h with biotinylated antisera raised against IgGs of the species of the first antibody (Vector Laboratories, Burlingame, CA, USA) diluted 1:500 in PBS, 0.3% Triton X-100, 1% BSA or normal serum. After four washes in PBS, sections were incubated for 2 h with avidin and biotinylated peroxidase complex (Vector Laboratories, Burlingame, CA, USA) diluted in PBS to 1:750 in IgG immunostaining and 1:500 in others. Finally, sections were transferred

264 to a sodium acetate buffer (0.1 M; pH 6.0) and stained using diaminobenzidine as a
265 chromogen in the presence of Ni-ions, thus yielding a dark grey to black precipitate.
266
267 *Microscopy and image analysis*
268 Staining reactions were stopped by rinses in sodium acetate and PBS, after which sections
269 were mounted on slides in 0.5% gelatin in distilled water containing chromo-potassium
270 sulphate, dehydrated in alcohol, defatted in xylene and coverslipped with Eukitt (O.Kindler
271 GmbH & CO, Freiburg, Brisgau, Germany). Stained sections were examined with a light-
272 microscope (Leica DM5500B, Leica Microsystems, Nanterre, France) and images were
273 captured by a high-resolution digital camera system (Leica DFC425C, Leica Microsystems,
274 Nanterre, France) and stored onto a personal computer. In every brain section between
275 bregma +4,85 and -2,85 mm the occurrence and extent (scored as restricted (1), intermediate
276 (2) or extensive (3)) of perivascular IgG diffusion in a given structure was noted. As each
277 region or structure considered covered at least two, but a varying number (depending on the
278 length of the structure), of brain sections (with two consecutive sections being separated by
279 240 μm), the number of occurrences of perivascular IgG diffusion for a structure were then
280 divided by the number of brain sections in which the structure was present. Similarly, the
281 cumulative score of the extent of IgG diffusion for a given brain region or structure was also
282 divided by the number of sections that contained the region or structure in question.
283 The counts and relative surfaces of AQP4, CNPase, COX-2, GFAP and Iba-1-
284 immunoreactive elements were quantified after application of fixed particle size and intensity
285 criteria on 8-bit images with Image J (http://imagej.nih.gov/ij/). Iba-1- and GFAP-
286 immunostaining was also quantified using the Image J plugin Fraclac
287 (http://rsb.info.nih.gov/ij/plugins/fraclac/fraclac.html). Briefly, on binary images of brain
288 sections between bregma -0.11 and -1.33 mm, Iba-1-positive cells (size between 300-6000

pixels) and GFAP-immunoreactive cells (size between 300-8000 pixels) were enclosed by a Hull convex (a boundary enclosing the foreground pixels of an image using straight line segments to each outermost point) and bounding circle after which the surface, perimeter, diameter and circularity (defined as $4*\pi*Area / Perimeter^2$) were determined in addition to the width and height of the cells. In addition, Iba-1 cell size and activation was also evaluated with Image J based on staining intensity as described by Hovens et al (2014). Briefly, a minimum size filter was applied on cell body size (>150 pixels) before cell and cell body size were distinguished based on an intensity criterion. Finally, three different categories of sizes of GFAP-positive elements (GFAP: <300 pixels considered as astrocytic fragments; 300<pixels<8000 considered as astrocytes; pixels>8000 considered as astrocytes in contact) were quantified in terms of number and relative surface after application of a fixed intensity threshold.

Image editing software (Adobe Photoshop, Adobe Systems, San Jose, CA, USA) was used only to adjust contrast and brightness for photomicrographs composing illustrating figures.

Data representation and analysis

Food intake and water intake were expressed relative to 100g of body weight and 100g of food intake respectively. Maximum intensity obtained from T2-weighted images analysis was expressed relative to skull muscle. To assess blood redistribution between brain structures, ASL values in cerebral structures were also expressed relative to perfusion of brain hemispheres or to that of the global brain parenchyma in the case of the corpus callosum that is situated between the two hemispheres. All data, except TBSS data, were expressed as means ± standard error of the mean (SEM) and analyzed by a one-way ANOVA with surgery as a between factor. When data were not normally distributed, a log10 or square root transformation was performed, and if still not normally distributed then the non-parametric

Mann-Whitney U test was used. Pearson linear correlation coefficients were calculated between MRI (T2, ASL and DTI) parameters and immunohistochemical (AQP4-, COX-2-, GFAP- and Iba-1-immunoreactivity) data. In all cases, a level of $p<0.05$ was considered as statistically significant.

For statistical analysis of TBSS data, a nonparametric voxel-wise statistical procedure was carried out using *randomise,* a permutation testing algorithm, with 500 and 5000 permutations. Threshold-free cluster enhancement (TFCE) method (Smith and Nichols, 2009) was used to define clusters with significant differences at $p < 0.05$ fully corrected for multiple comparisons across space. Contrasts were performed for sham-operated vs. CLP animals. TBSS results were displayed on top of the group mean_FA map, the DTI-RAPnD72_template and the DTI-RAPnD72_labels.

Results

CLP reduced food intake and induced encephalopathy

Within the 23h following the end of surgery, no mortality was observed in the sham-operated group (One animal did die however at the induction of anesthesia for imaging) while CLP resulted in 12.5% mortality. One-way ANOVAs on food consumption relative to body weight during the 24h before surgery did not reveal any differences between animals to be allocated to treatment groups. However, a Mann-Whitney U-test on food consumption relative to body weight during the 24h after the start of surgery showed a significant lower food intake in animals that underwent CLP as compared to sham-operated rats (U: 26.0, $p<0.05$) (Fig. 2A). Mann-Whitney tests on corneal, pinna and righting reflexes showed that CLP significantly reduced the righting reflex 8 (U: 10.0, $p<0.001$) and 24h (U: 4.50, $p<0.001$) later as compared to sham surgery (Fig. 2B) without affecting the pinna and corneal reflexes (Fig. 2C, D).

CLP increased T2-weighted intensities in cortex and striatum

One way ANOVAs on T2-weighted intensity ratios (VOIs of interest relative to that of skull muscle) showed significantly greater maximum and average intensities at the base of the brain ($F_{1,17}$: 8.98, $p<0.01$; Fig. 3A; $F_{1,17}$: 16.4, $p<0.001$ (data not shown), respectively) in CLP animals as compared to sham-operated rats. Similar analyses in the cortex also indicated a greater maximum ($F_{1,18}$: 5.41, $p<0.05$; Fig. 3B) in CLP rats compared to sham-surgery controls, but no effect on average intensity. In the striatum, one way ANOVAs showed greater maximum and average intensities ($F_{1,18}$: 5.39, $p<0.05$; Fig. 3C; $F_{1,18}$: 6.99, $p<0.05$ (data not shown), respectively) 24h after CLP compared to sham-surgery. Finally, one way ANOVAs only revealed a trend for an increased maximum in the corpus callosum ($F_{1,18}$: 4.08, $p=0.059$; Fig. 3D) of CLP animals as compared to sham-operated rats with no differences in average intensities.

352

353 *CLP decreased perfusion towards the cerebral cortex*

354 One-way ANOVAs or Mann-Whitney tests on absolute perfusion values in the ROIs
355 covering the cortex (Sham: 105.75 ± 7.29ml/100g/min; CLP: 97.97 ± 5.46ml/100g/min),
356 striatum (Sham 102.56 ± 10.71ml/100g/min; CLP: 96.7 ± 7.24ml/100g/min), corpus callosum
357 (Sham: 112.85 ± 9.07ml/100g/min; CLP 101.28 ± 7.77ml/100g/min) and external capsule
358 (Sham: 94.21 ± 8.48ml/100g/min; CLP 87.07 ± 4.88ml/100g/min) did not reveal significant
359 differences between CLP- and sham surgery groups 24 h after surgery.

360 To assess the distribution of blood between brain structures, perfusion values measured in
361 brain areas were also analyzed relative to that of the hemisphere (or to that of the global brain
362 parenchyma in the case of the ROI centered on the corpus callosum that is situated between
363 the two hemispheres). One-way ANOVAs on these data indicated significant lower
364 distribution of blood to the cortex ($F_{1,18}$: 5.04, $p<0.05$; Fig. 4A), but no changes in perfusion
365 distribution to the striatum (Fig. 4B), corpus callosum (Fig. 4C) or external capsule region
366 (Fig. 4D) in animals that had undergone CLP surgery as compared to sham surgery.

367

368 *CLP increased axial water diffusion in the corpus callosum*

369 DWI data were generally of good comparable quality in 20 out of 21 animals. One animal
370 was excluded because its head was tilted in a way that hindered processing for DTI.

371 Mann-Whitney tests on water diffusion parameters in the ROI covering the cortex at the
372 anatomical level where the white matter of the anterior commissure crosses the third ventricle
373 (corresponding to bregma -0.51mm (Swanson, 1998)) or at the level where the third ventricle
374 is divided in a ventral and dorsal part by the grey matter of the paraventricular thalamus,
375 (corresponding to bregma -1.08mm (Swanson, 1998)) did not indicate any significant
376 differences between rats that underwent CLP and those that were subject to sham surgery.

Similar analyses on water diffusion parameters in the striatum ROI indicated a significant decrease in RD at bregma -1.08mm ($F_{1,18}$: 4.82, $p<0.05$). Using a non-hypothesis-driven and non-ROI-based TBSS approach, a significant higher FA was found in the ventral caudate putamen and globus pallidus of images centered at bregmas -0.51 and -0.83mm of CLP rats as compared to sham-operated animals after 5000 random permutations (Supplementary fig. 1).

One-way ANOVAs or Mann-Whitney tests on water diffusion parameters measured in the corpus callosum ROI at bregma -0.51mm indicated a significant increase in λ1 (U: 19.0, $p<0.05$; Fig. 5A) and a significant decrease in Cp (U: 18.0, $p<0.05$) in rats that underwent CLP surgery as compared to sham-operated rats.

Finally, one-way ANOVAs or Mann-Whitney tests on water diffusion parameters in the ROI placed on the external capsule at bregma -1.08mm revealed a significant increase in FA in the left external capsule ($F_{1,18}$: 5.33, $p<0.05$; Fig. 5B) after CLP as compared to sham surgery.

CLP did not induce widespread BBB breakdown

In all animals, IgG was found in brain regions lacking a functional BBB including the choroid plexus, meninges and circumventricular organs from which it spread to surrounding regions (Fig. 6A, B). One-way ANOVA or Mann-Whitney tests on the occurrence of perivascular plume-like diffusion clouds of IgG staining in the white matter revealed a significantly increased frequency in the fimbria (U: 30.0, $p<0.05$; not shown), but not in the corpus callosum (Fig. 6C, D) or elsewhere in the white matter (Fig. 6E, F), of rats that underwent sham surgery as compared to CLP animals. Similar analyses on grey matter did not indicate any differences with regard to the light to moderate perivascular IgG diffusion that was occasionally observed in the cortex, striatum and hippocampus of both sham-operated and CLP animals (Fig. 6G-J).

CLP decreased cortical COX-2-immunoreactivity

No or very weak COX-2 immunoreactivity was found associated with blood vessels in the preoptic area (Fig. 7A), caudate putamen (Fig. 7C), external capsule (Fig. 7E), hippocampus (Fig. 7G) or cortex (Fig. 7I) of animals subjected to sham-surgery. However, distinct perivascular disc-like COX-2-immunoreactive cells were frequently observed in these structures, with the exception of the hippocampus, in rats that underwent CLP (Fig. 7B, D, F, H and J).

Constitutive COX-2 expression was detected in neurons of the hippocampus and to a lesser extent, in neurons of the cortex (Fig. 7 G-J). Interestingly, and in spite of perivascular induction of COX-2 in the cortex, one-way ANOVAs on cortical COX-2-immunoreactivity showed a significant decrease in the number of cells ($F_{1,11}$: 22.2, $p<0.001$), the total ($F_{1,11}$: 8.37, $p<0.05$) and relative ($F_{1,11}$: 8.90, $p<0.05$) surface labeled after CLP in comparison to sham-surgery (Fig. 7K, L). Interestingly, significant positive correlations were found between the total and relative surface occupied by COX-2 immunoreactivity and perfusion distribution to the cortex (both $r=0.75$, $p<0.005$).

CLP altered microglial density and morphology in grey and white matter

One-way ANOVAs on Iba-1 staining in the cortex revealed a significant increase in the number ($F_{1,15}$: 8.68, $p<0.05$) and relative surface ($F_{1,15}$: 7.46, $p<0.05$) of positive elements in CLP rats compared to sham-operated animals. Similar analyses on Iba-1-immunoreactivity in the striatum also indicated a significant increase in number ($F_{1,16}$: 6.15, $p<0.05$) and relative surface labeled ($F_{1,16}$: 6.29, $p<0.05$) after CLP rats as compared to sham surgery. In addition, one-way ANOVAs on Iba-1 staining in the ventral part of the striatum at bregma levels -0.51 to -0.83mm, that was indicated by tract-based spatial statistics of water diffusion data,

427 indicated a significant increase in relative surface ($F_{1,16}$: 5.48, $p<0.05$) of positive elements in
428 CLP rats as compared to sham-operated animals. Finally, a significant negative correlation
429 was found between the number of Iba-1-immunoreactive elements and MD in the striatum at
430 bregma -1.08mm ($r=-0.50$, $p<0.05$).
431 In contrast, one-way ANOVAs on Iba-1 staining in the corpus callosum (Fig. 8A, B) did not
432 reveal a significant difference in relative surface of positive elements in CLP rats as
433 compared to sham-operated animals. However, one-way ANOVAs or Mann-Whitney tests on
434 other measures obtained by fractal analysis showed a significant increase in area (U: 21.0,
435 $p<0.05$), perimeter ($U=21.0$, $p<0.05$), height ($F_{1,18}$: 14.9, $p<0.01$; Fig. 8C) and width ($F_{1,18}$:
436 6.93, $p<0.05$; Fig. 8D) of Iba-1-positive elements in CLP rats compared to sham-operated
437 animals. One-way ANOVAs or Mann-Whitney tests on parameters generated by the method
438 of Hovens et al. (2014) indicated a significant decrease in Iba-1-positive cell size (U:18.0,
439 $p<0.05$) and cell processes (U: 18.0, $p<0.05$) and a significantly increased cell body size (U:
440 0.0, $p<0.001$) as well as a significantly increased microglial activation measure (cell body
441 size/cell size; $F_{1,17}$: 6.94, $p<0.05$) in CLP animals compared to sham-operated rats. Linear
442 regression analyses did not indicate any significant correlations between measures of Iba-1-
443 immunoreactivity and increased axial diffusion in the corpus callosum.
444
445 *CLP altered corpus callosum astroglia morphology, but not density*
446 One-way ANOVAs on GFAP staining in the cortex revealed a significant increase in the
447 number ($F_{1,19}$: 4.91, $p<0.05$) and relative surface ($F_{1,19}$: 4.55, $p<0.05$) of positive elements in
448 CLP rats compared to sham-operated animals. Similar analyses on GFAP-immunoreactivity
449 in the striatum also indicated a significant increase in number ($F_{1,19}$: 6.14, $p<0.05$) and
450 relative surface labeled ($F_{1,19}$: 5.82, $p<0.05$) in after CLP as compared to sham surgery.
451 Finally, a one-way ANOVA on GFAP staining in the ventral region of the striatum at bregma

452 levels -0.51 and -0.83mm, indicated by tract-based spatial statistics to show changes in water
453 diffusion, showed a trend for an increase in number ($F_{1,13}$: 4.57, p=0.052) of GFAP-positive
454 elements.
455 One-way ANOVAs or Mann-Whitney tests on GFAP staining in the corpus callosum (Fig.
456 9A, B) did not reveal any differences in number or relative surface of positive elements
457 between CLP rats and sham-operated animals. One-way ANOVAs on fractal parameters of
458 GFAP-1-positive cells in the corpus callosum also did not indicate significant differences in
459 height (Fig. 9C), width, perimeter, surface and circularity.
460 One-way ANOVAs on GFAP-positive fragments (<300 pixels) in the corpus callosum using
461 a fixed threshold did however indicate a significantly lower number of counts ($F_{1,17}$: 8.45,
462 $p<0.05$) and relative surface ($F_{1,17}$: 18.49, $p<0.001$; Fig. 9D) in the CLP group as compared to
463 sham surgery. Interestingly, significant negative correlations were found between the number
464 of and the relative surface occupied by GFAP-positive fragments and axial water diffusion
465 ($r=-0.63$, $p<0.01$ and $r=-0.70$, $p<0.005$, respectively) in the corpus callosum.
466
467 *CLP decreased cortical AQP4 expression*
468 One way ANOVA showed that cortical AQP4-immunoreactivity (Fig. 10A, B) between
469 bregma -0.46 and -1.08 mm, which corresponded to the position of the T2-weighted image
470 analyzed above, was significantly lower 24h after CLP-induced sepsis than after sham
471 surgery in terms of both counts ($F_{1,14}$:9.74, $p<0.01$; Fig. 10C) and relative surface ($F_{1,14}$:8.66,
472 $p<0.05$; Fig. 10D). Similar analyses on AQP4-positive staining in the corpus callosum and
473 striatum did not indicate differences between groups. In addition, no significant correlations
474 were found between AQP4-immunoreactivity and T2-weighted images in any of these brain
475 structures.

Discussion

The main findings of the present work were that CLP induced sepsis-associated CNS dysfunction resulted in higher T2-weighted contrast intensities in the cortex, striatum and at the base of the brain, decreased blood perfusion distribution to the cortex and increased axial water diffusion in the corpus callosum and fractional anisotropy in the ventral striatum compared to sham surgery. In these animals, CLP induced perivascular COX-2 expression, decreased cortical COX-2 and AQP4 expression and altered white matter glial cell morphology. Interestingly, positive correlations were established between COX-2 immunoreactivity and perfusion distribution to the cortex, while negative correlations were found between GFAP-positive fragments and axial water diffusion in the corpus callosum.

Decreased food intake is a classic non-specific symptom of systemic inflammation in response to bacterial infection (Hart, 1988; Konsman and Dantzer, 2001) and was observed following CLP. In addition, the loss of the righting reflex in animals that underwent CLP is in agreement with previous studies (Kadoi and Goto, 2004; Kafa et al., 2010a; Kafa et al., 2010b) and indicated deteriorated neurological status and SAE**.**

Using the perivascular diffusion of IgG as a marker of BBB breakdown, no indication of increased BBB permeability was found in the parenchyma of the grey and white matter, except for the fimbria, after CLP in the present work. This was neither due to technical failure nor lack of sensitivity as perivascular IgG was readily observed in brain circumventricular organs and meninges, where the endothelial BBB is absent. Moreover, we recently showed increased perivascular IgG diffusion in the white matter after ip LPS administration using the same staining protocol (Dhaya et al., 2018). It is important to keep in mind however that the severity of CLP-induced sepsis depends on the size of the needle used to puncture as well as the number of punctures (Rittirsch et al., 2009) and that the needle size used here was smaller than previous work reporting BBB breakdown 24h after CLP in rodents (Avtan et al., 2011;

Comim et al., 2011; Imamura et al., 2011; Jeppson et al., 1981; Vachharajani et al., 2012; Yokoo et al., 2012). Given that SAE has been proposed to be related to BBB breakdown (Chaudhry and Duggal, 2014; Papadopoulos et al., 2000; Tsuruta and Oda, 2016), our experimental model is interesting in that it induces signs of neurological impairment in the absence of widespread BBB breakdown for molecules of high molecular weight.

Behavioral impairment was associated with signs of fluid accumulation at the base of the brain as indicated by increased T2-weighted contrast, which is in accordance with results of T2-weighted imaging in a murine CLP model (Bozza et al., 2010). In addition, increased T2-weighted contrast intensities were also found in the cortex and striatum in the present work. As diffusion imaging did not indicate altered ADC in the cortex and striatum the increase in T2 intensities were considered as indicating vasogenic rather than cytotoxic edema (Loubinoux et al., 1997). Interestingly, lower perivascular expression of the water channel AQP4 was observed in the cortex of CLP animals as compared to those subject to sham surgery. Reduced water clearance may therefore, in part, explain the increased T2-weighted contrast intensity found in the cortex after CLP.

Since in addition to edema, SAE has been proposed to be related to reduced CBF and oxygen extraction (Papadopoulos et al., 2000), the perfusion of major brain was assessed with ASL. The accuracy of ASL-FAIR to quantify brain perfusion in the rat at low, normal, and moderately increased flows has been validated by a direct comparison with the cerebral distribution of intravenously-injected radioactive microspheres (Bos et al., 2012). Brain perfusion values in sham-operated animals were in accordance with those observed in some previous studies (Detre et al., 1992; Williams et al., 1992), but higher than those described by others (Danker and Duong, 2007; Shen et al., 2016), yet lower than measured in still other published work (Carr et al., 2007; Moffat et al., 2005; Williams et al., 1992). These discrepancies may be due to differences in anesthesia, ASL sequences used and the way the

brain was defined (in our case both cerebral hemispheres without the ventricular system and the large vessels at the base of the brain). This being said, ASL-based perfusion data are known to vary even between studies of the same group (Danker and Duong, 2007; Shen et al., 2016; Sicard et al., 2003) and the aim of the present work was not to obtain absolute quantitative, but to compare between CLP and sham-surgery.

Like in our previous work with LPS (Dhaya et al., 2018), perfusion of the global brain, striatum and cortex was not found to be altered by CLP-induced sepsis. In addition, to absolute perfusion values, the distribution of blood between brain structures is an important value as this distribution can vary as a function of local cerebral metabolism. In this respect it is interesting to note that the distribution of blood to the cortex relative to that of the ipsilateral hemisphere was lower 24h after CLP as compared to sham-surgery. This relative hypoperfusion of the cortex may be related to a loss of cerebral autoregulation or uncoupling between CBF and cerebral metabolism (Feng et al., 2010; Rosengarten et al., 2007). The reported local decrease of glucose utilization in cortical areas (Soejima et al., 1990) and altered cortical electric activity (Kafa et al., 2010a) during sepsis support the possibility of altered cortical metabolism. Cortical COX-2 plays an important role in neurovascular coupling between neuronal activity and CBF (Niwa et al., 2000; Stefanovic et al., 2006). Interestingly although increased perivascular *de novo* induction of perivascular COX-2 was observed after CLP, overall cortical COX-2-immunoreactivity was decreased as compared to sham-surgery. Moreover, significant positive correlations were found between the total and relative surface occupied by COX-2 immunoreactivity and perfusion distribution to the cortex indicating that these imaging and histological measures varied to the same extent. Thus, decreased neuronal COX-2 may explain the observed decrease in blood distribution towards the cerebral cortex during sepsis.

In accordance with and expanding our previous work on LPS, increased axial water diffusion

552 was observed in the body of corpus callosum after CLP. The body of the corpus callosum is
553 characterized by large axonal diameter distribution and a higher diffusivity suggesting that
554 the space between axons may be larger than that in the genu and splenium where axonal
555 diameter is lower (Barazany et al., 2009). The observed decrease in the coefficient of planar
556 anisotropy in the corpus callosum may also be explained by increased axial water diffusion as
557 $\lambda 1$ is part of the divider term that allows to calculate planar anisotropy ($Cp = 2(\lambda 2 - \lambda 3)/(\lambda 1 +$
558 $\lambda 2 + \lambda 3)$). Of note, septic patients that had suffered from SAE show an inverse correlation
559 between delirium duration and FA in the body of the corpus callosum three months later, but
560 not at hospital discharge (Morandi et al., 2012). The shape-oriented anisotropy measure Cp
561 has been shown to be more useful than FA to differentiate between white matter fibers and
562 abscesses, between white matter and tumors and between invasive and well-demarcated
563 tumors in the brain (Kim et al., 2008; Kumar et al., 2008; Lope-Piedrafita et al., 2008).
564 Collectively, previously-published findings together with the present observations suggest
565 that during inflammation axial diffusion increases while planar anisotropy decreases in the
566 white matter of the corpus callosum first to later give rise to decreased fractional anisotropy.
567 However, lower FA in the splenium and genu, but not in the body, of the corpus callosum at
568 hospital discharge is associated with worse verbal fluency and attention scores months later
569 (Morandi et al., 2012). Interestingly, patients with PTSD, a condition that also often occurs
570 months after sepsis (Boer et al., 2008; Rosendahl et al., 2013; Schelling et al., 2001;
571 Wintermann et al., 2015), do show decreased FA in the body of the corpus callosum when
572 compared with healthy non-trauma-exposed controls as well as a negative correlation
573 between PTSD clinical scores and the corpus callosum body FA (O'Doherty et al., 2018).
574 Thus, our present findings of reduced planar anisotropy in the corpus callosum body 24h after
575 sepsis induction may be relevant for the subsequent of development stress disorder but not for
576 that of cognitive impairment.

577 Recently, disruption of the tubulin network inside white matter axons has been shown in rats
578 made septic by intraperitoneal injection of fecal slurry (Ehler et al., 2017). If the same
579 phenomenon occurred after CLP, this could alter axial diffusion in the corpus callosum.
580 Interestingly, peripheral administration of the microtubule assembly inhibitor methylmercury
581 increases axial diffusion in rat optic nerves (Kinoshita et al., 1999) and suggests that the
582 increase in axial diffusion as observed in the corpus callosum of septic animals could be
583 related to changes in the intraneuronal tubulin network. Alternatively, retraction of the
584 processes of microglia or astrocytes that occupy the space between white mater fibers may
585 explain increased horizontal water diffusion in the corpus callosum after CLP. Indeed, in the
586 corpus callosum, microglia and astrocytes have several long cytoplasmic processes that run
587 mostly parallel, but also perpendicularly to the longitudinal axis of myelinated axons
588 (Lawson et al., 1990; Mori and Leblond, 1969a, b). In the present work, an increase in Iba-1
589 positive cell body size, a decrease in cell processes stained for Iba-1and an increase in cell
590 body to cell size ratio were observed in the corpus callosum of CLP animals as compared to
591 that of rats that underwent sham-surgery. This increased cell body to cell size ratio has been
592 proposed as a measure of microglial activation (Hovens et al., 2014). In addition, CLP
593 decreased in the number of GFAP-positive fragments in the corpus callosum. The decrease in
594 Iba-1 positive cell processes and GFAP-immunoreactive fragments may represent retraction
595 of glial processes. This retraction would result in less hindrance for axial water diffusion in
596 the corpus callosum and thus increase it.
597 When white matter astrocytes are activated, they retract their higher order processes, increase
598 their soma and lose their transverse orientation (Sun et al., 2010). Less GFAP-
599 irmmunorreactive fragments were found in the corpus callosum after CLP than after sham-
600 surgery. Interestingly, significant negative correlations were found between the number of as
601 well as the relative surface occupied by GFAP-positive fragments and axial water diffusion in

602 the corpus callosum suggesting that changes in this astrocytic marker underlie, at least in part,
603 the observed modifications of dMRI parameters. Although GFAP does not mark astrocytic
604 endfeet (Sun and Jakobs, 2012), this finding can be interpreted to suggest astroglial activation
605 and retraction of their processes, which, like for microglia, allows for increased diffusion of
606 water molecules parallel to corpus callosum fibers.
607 One of the main differences between the present small animal imaging approach and previous
608 clinical imaging studies on sepsis is the use of anesthesia to prevent movement at the level of
609 the brain. While the effects of isoflurane anesthesia on rodent regional cerebral blood flow is
610 relatively well-known (Sicard et al., 2003), to the best of our knowledge no comparison of
611 white matter diffusion MRI parameters between isoflurane anesthetized and awake rodents
612 has been done to date. Future work will need to address this matter and determine to what
613 extent the present findings are translationally relevant. If the effects of anesthesia turn out to
614 be negligible, then longitudinal MRI studies of experimental SAE can be envisioned.
615 In conclusion, our findings confirm the existence of brain dysfunction and increased T2-
616 weighted contrast at the base of the brain 24 h after CLP in rodents. In addition, they expand
617 previous findings in showing increased T2-weighted contrast in the striatum and cortex,
618 decreased perfusion distribution to the cortex and increased axial water diffusion in the
619 corpus callosum. Importantly, these imaging findings were accompanied by lower numbers
620 of Iba-1- and GFAP-immunoreactive fragments in the corpus callosum, decreased neuronal
621 COX-2 and AQP4 expression in the cortex, but not by widespread perivascular IgG diffusion
622 indicating breakdown of the BBB. Collectively, these findings indicate that early SAE is
623 related to changes in cerebral blood flow and white matter microstructure, but not to BBB
624 breakdown.
625
626 **Acknowledgements**

627 This work was supported by public grants from the French Agence Nationale de la Recherche
628 within the context of the Investments for the Future program referenced ANR-10-LABX-57
629 named TRAIL (project HR-dMRI).

631 **References**

632 Abdel-Aty, H., Boye, P., Zagrosek, A., Wassmuth, R., Kumar, A., Messroghli, D., Bock, P.,
633 Dietz, R., Friedrich, M.G., Schulz-Menger, J., 2005. Diagnostic performance of
634 cardiovascular magnetic resonance in patients with suspected acute myocarditis:
635 comparison of different approaches. J Am Coll Cardiol 45, 1815-1822.
636 Alexander, A.L., Hasan, K., Kindlmann, G., Parker, D.L., Tsuruda, J.S., 2000. A geometric
637 analysis of diffusion tensor measurements of the human brain. Magn Reson Med 44,
638 283-291.
639 Avtan, S.M., Kaya, M., Orhan, N., Arslan, A., Arican, N., Toklu, A.S., Gurses, C., Elmas, I.,
640 Kucuk, M., Ahishali, B., 2011. The effects of hyperbaric oxygen therapy on blood-brain
641 barrier permeability in septic rats. Brain Res 1412, 63-72.
642 Barazany, D., Basser, P.J., Assaf, Y., 2009. In vivo measurement of axon diameter
643 distribution in the corpus callosum of rat brain. Brain 132, 1210-1220.
644 Bartynski, W.S., Boardman, J.F., Zeigler, Z.R., Shadduck, R.K., Lister, J., 2006. Posterior
645 reversible encephalopathy syndrome in infection, sepsis, and shock. AJNR Am J
646 Neuroradiol 27, 2179-2190.
647 Boer, K.R., van Ruler, O., van Emmerik, A.A., Sprangers, M.A., de Rooij, S.E., Vroom,
648 M.B., de Borgie, C.A., Boermeester, M.A., Reitsma, J.B., Dutch Peritonitis Study, G.,
649 2008. Factors associated with posttraumatic stress symptoms in a prospective cohort of
650 patients after abdominal sepsis: a nomogram. Intensive Care Med 34, 664-674.
651 Bos, A., Bergmann, R., Strobel, K., Hofheinz, F., Steinbach, J., den Hoff, J., 2012. Cerebral
652 blood flow quantification in the rat: a direct comparison of arterial spin labeling MRI
653 with radioactive microsphere PET. EJNMMI Res 2, 47.
654 Bowton, D.L., Bertels, N.H., Prough, D.S., Stump, D.A., 1989. Cerebral blood flow is
655 reduced in patients with sepsis syndrome. Crit Care Med 17, 399-403.

656 Bozza, F.A., Garteiser, P., Oliveira, M.F., Doblas, S., Cranford, R., Saunders, D., Jones, I.,
657 Towner, R.A., Castro-Faria-Neto, H.C., 2010. Sepsis-associated encephalopathy: a
658 magnetic resonance imaging and spectroscopy study. J Cereb Blood Flow Metab 30,
659 440-448.
660 Bryan, W.J., Emerson, T.E., Jr., 1977. Blood flow in seven regions of the brain during
661 endotoxin shock in the dog. Proc Soc Exp Biol Med 156, 205-208.
662 Carr, J.P., Buckley, D.L., Tessier, J., Parker, G.J., 2007. What levels of precision are
663 achievable for quantification of perfusion and capillary permeability surface area
664 product using ASL? Magn Reson Med 58, 281-289.
665 Chaudhry, N., Duggal, A.K., 2014. Sepsis Associated Encephalopathy. Adv Med 2014,
666 762320.
667 Christenson, J.T., Kuikka, J.T., Owunwanne, A., Al-Sarraf, A.A., 1986. Cerebral circulation
668 during endotoxic shock with special emphasis on the regional cerebral blood flow in
669 vivo. Nucl Med Commun 7, 531-540.
670 Comim, C.M., Vilela, M.C., Constantino, L.S., Petronilho, F., Vuolo, F., Lacerda-Queiroz,
671 N., Rodrigues, D.H., da Rocha, J.L., Teixeira, A.L., Quevedo, J., Dal-Pizzol, F., 2011.
672 Traffic of leukocytes and cytokine up-regulation in the central nervous system in sepsis.
673 Intensive Care Med 37, 711-718.
674 Danker, J.F., Duong, T.Q., 2007. Quantitative regional cerebral blood flow MRI of animal
675 model of attention-deficit/hyperactivity disorder. Brain Res 1150, 217-224.
676 Detre, J.A., Leigh, J.S., Williams, D.S., Koretsky, A.P., 1992. Perfusion imaging. Magn
677 Reson Med 23, 37-45.
678 Dhaya, I., Griton, M., Raffard, G., Amri, M., Hiba, B., Konsman, J.P., 2018. Bacterial
679 lipopolysaccharide-induced systemic inflammation alters perfusion of white matter-rich
680 regions without altering flow in brain-irrigating arteries: Relationship to blood-brain

barrier breakdown? J Neuroimmunol 314, 67-80.

Dobre, M.C., Ugurbil, K., Marjanska, M., 2007. Determination of blood longitudinal relaxation time (T1) at high magnetic field strengths. Magn Reson Imaging 25, 733-735.

Ebersoldt, M., Sharshar, T., Annane, D., 2007. Sepsis-associated delirium. Intensive Care Med 33, 941-950.

Ehler, J., Barrett, L.K., Taylor, V., Groves, M., Scaravilli, F., Wittstock, M., Kolbaske, S., Grossmann, A., Henschel, J., Gloger, M., Sharshar, T., Chretien, F., Gray, F., Noldge-Schomburg, G., Singer, M., Sauer, M., Petzold, A., 2017. Translational evidence for two distinct patterns of neuroaxonal injury in sepsis: a longitudinal, prospective translational study. Crit Care 21, 262.

Ekstrom-Jodal, B., Haggendal, J., Larsson, L.E., Westerlind, A., 1982. Cerebral hemodynamics, oxygen uptake and cerebral arteriovenous differences of catecholamines following E. coli endotoxin in dogs. Acta Anaesthesiol Scand 26, 446-452.

Esparza-Coss, E., Wosik, J., Narayana, P.A., 2010. Perfusion in rat brain at 7 T with arterial spin labeling using FAIR-TrueFISP and QUIPSS. Magn Reson Imaging 28, 607-612.

Feng, S.Y., Samarasinghe, T., Phillips, D.J., Alexiou, T., Hollis, J.H., Yu, V.Y., Walker, A.M., 2010. Acute and chronic effects of endotoxin on cerebral circulation in lambs. Am J Physiol Regul Integr Comp Physiol 298, R760-766.

Gofton, T.E., Young, G.B., 2012. Sepsis-associated encephalopathy. Nat Rev Neurol 8, 557-566.

Hart, B.L., 1988. Biological basis of the behavior of sick animals. Neurosci Biobehav Rev 12, 123-137.

Hinkelbein, J., Schroeck, H., Peterka, A., Schubert, C., Kuschinsky, W., Kalenka, A., 2007. Local cerebral blood flow is preserved in sepsis. Curr Neurovasc Res 4, 39-47.

Hoogland, I.C., Houbolt, C., van Westerloo, D.J., van Gool, W.A., van de Beek, D., 2015.

706 Systemic inflammation and microglial activation: systematic review of animal
707 experiments. J Neuroinflammation 12, 114.
708 Hovens, I.B., Nyakas, C., Schoemaker, R.G., 2014. A novel method for evaluating microglial
709 activation using ionized calcium□binding adaptor protein□1 staining: cell body to cell
710 size ratio. Neuroimmunol Neuroinflammation 1, 82-88.
711 Imamura, Y., Wang, H., Matsumoto, N., Muroya, T., Shimazaki, J., Ogura, H., Shimazu, T.,
712 2011. Interleukin-1beta causes long-term potentiation deficiency in a mouse model of
713 septic encephalopathy. Neuroscience 187, 63-69.
714 Jeppson, B., Freund, H.R., Z., G., James, J.H., von Meyenfeldt, M.F., J.E., F., 1981. Blood-
715 brain barrier derangement in sepsis: cause of septic encephalopathy? Am J Surg 141,
716 136-142.
717 Jones, C., Griffiths, R.D., 2013. Mental and physical disability after sepsis. Minerva
718 Anestesiol 79, 1306-1312.
719 Kadoi, Y., Goto, F., 2004. Selective inducible nitric oxide inhibition can restore
720 hemodynamics, but does not improve neurological dysfunction in experimentally-
721 induced septic shock in rats. Anesth Analg 99, 212-220.
722 Kafa, I.M., Bakirci, S., Uysal, M., Kurt, M.A., 2010a. Alterations in the brain electrical
723 activity in a rat model of sepsis-associated encephalopathy. Brain Res 1354, 217-226.
724 Kafa, I.M., Uysal, M., Bakirci, S., Ayberk Kurt, M., 2010b. Sepsis induces apoptotic cell
725 death in different regions of the brain in a rat model of sepsis. Acta Neurobiol Exp
726 (Wars) 70, 246-260.
727 Kim, S., Pickup, S., Hsu, O., Poptani, H., 2008. Diffusion tensor MRI in rat models of
728 invasive and well-demarcated brain tumors. NMR Biomed 21, 208-216.
729 Kinoshita, Y., Ohnishi, A., Kohshi, K., Yokota, A., 1999. Apparent diffusion coefficient on
730 rat brain and nerves intoxicated with methylmercury. Environ Res 80, 348-354.

731 Kober, F., Iltis, I., Izquierdo, M., Desrois, M., Ibarrola, D., Cozzone, P.J., Bernard, M., 2004.
732 High-resolution myocardial perfusion mapping in small animals in vivo by spin-labeling
733 gradient-echo imaging. Magn Reson Med 51, 62-67.
734 Konsman, J.P., Blomqvist, A., 2005. Forebrain patterns of c-Fos and FosB induction during
735 cancer-associated anorexia-cachexia in rat. Eur J Neurosci 21, 2752-2766.
736 Konsman, J.P., Dantzer, R., 2001. How the immune and nervous systems interact during
737 disease-associated anorexia. Nutrition 17, 664-668.
738 Konsman, J.P., Veeneman, J., Combe, C., Poole, S., Luheshi, G.N., Dantzer, R., 2008.
739 Central nervous action of interleukin-1 mediates activation of limbic structures and
740 behavioural depression in response to peripheral administration of bacterial
741 lipopolysaccharide. Eur J Neurosci 28, 2499-2510.
742 Konsman, J.P., Vigues, S., Mackerlova, L., Bristow, A., Blomqvist, A., 2004. Rat brain
743 vascular distribution of interleukin-1 type-1 receptor immunoreactivity: relationship to
744 patterns of inducible cyclooxygenase expression by peripheral inflammatory stimuli. J
745 Comp Neurol 472, 113-129.
746 Kumar, M., Gupta, R.K., Nath, K., Rathore, R.K., Bayu, G., Trivedi, R., Husain, M., Prasad,
747 K.N., Tripathi, R.P., Narayana, P.A., 2008. Can we differentiate true white matter fibers
748 from pseudofibers inside a brain abscess cavity using geometrical diffusion tensor
749 imaging metrics? NMR Biomed 21, 581-588.
750 Lamar, C.D., Hurley, R.A., Taber, K.H., 2011. Sepsis-associated encephalopathy: review of
751 the neuropsychiatric manifestations and cognitive outcome. J Neuropsychiatry Clin
752 Neurosci 23, 237-241.
753 Lawson, L.J., Perry, V.H., Dri, P., Gordon, S., 1990. Heterogeneity in the distribution and
754 morphology of microglia in the normal adult mouse brain. Neuroscience 39, 151-170.
755 Lemstra, A.W., Groen in't Woud, J.C., Hoozemans, J.J., van Haastert, E.S., Rozemuller, A.J.,

Eikelenboom, P., van Gool, W.A., 2007. Microglia activation in sepsis: a case-control study. J Neuroinflammation 4, 4.

Lope-Piedrafita, S., Garcia-Martin, M.L., Galons, J.P., Gillies, R.J., Trouard, T.P., 2008. Longitudinal diffusion tensor imaging in a rat brain glioma model. NMR Biomed 21, 799-808.

Loubinoux, I., Volk, A., Borredon, J., Guirimand, S., Tiffon, B., Seylaz, J., Meric, P., 1997. Spreading of vasogenic edema and cytotoxic edema assessed by quantitative diffusion and T2 magnetic resonance imaging. Stroke 28, 419-426; discussion 426-417.

Maekawa, T., Fujii, Y., Sadamitsu, D., Yokota, K., Soejima, Y., Ishikawa, T., Miyauchi, Y., Takeshita, H., 1991. Cerebral circulation and metabolism in patients with septic encephalopathy. Am J Emerg Med 9, 139-143.

Meagher, D.J., Morandi, A., Inouye, S.K., Ely, W., Adamis, D., Maclullich, A.J., Rudolph, J.L., Neufeld, K., Leonard, M., Bellelli, G., Davis, D., Teodorczuk, A., Kreisel, S., Thomas, C., Hasemann, W., Timmons, S., O'Regan, N., Grover, S., Jabbar, F., Cullen, W., Dunne, C., Kamholz, B., Van Munster, B.C., De Rooij, S.E., De Jonghe, J., Trzepacz, P.T., 2014. Concordance between DSM-IV and DSM-5 criteria for delirium diagnosis in a pooled database of 768 prospectively evaluated patients using the delirium rating scale-revised-98. BMC Med 12, 164.

Moffat, B.A., Chenevert, T.L., Hall, D.E., Rehemtulla, A., Ross, B.D., 2005. Continuous arterial spin labeling using a train of adiabatic inversion pulses. J Magn Reson Imaging 21, 290-296.

Moller, K., Strauss, G.I., Qvist, J., Fonsmark, L., Knudsen, G.M., Larsen, F.S., Krabbe, K.S., Skinhoj, P., Pedersen, B.K., 2002. Cerebral blood flow and oxidative metabolism during human endotoxemia. J Cereb Blood Flow Metab 22, 1262-1270.

Morandi, A., Rogers, B.P., Gunther, M.L., Merkle, K., Pandharipande, P., Girard, T.D.,

781 Jackson, J.C., Thompson, J., Shintani, A.K., Geevarghese, S., Miller, R.R., 3rd,
782 Canonico, A., Cannistraci, C.J., Gore, J.C., Ely, E.W., Hopkins, R.O., Visions
783 Investigation, V.I.S.N.S., 2012. The relationship between delirium duration, white
784 matter integrity, and cognitive impairment in intensive care unit survivors as determined
785 by diffusion tensor imaging: the VISIONS prospective cohort magnetic resonance
786 imaging study*. Crit Care Med 40, 2182-2189.
787 Mori, S., Leblond, C.P., 1969a. Electron microscopic features and proliferation of astrocytes
788 in the corpus callosum of the rat. J Comp Neurol 137, 197-225.
789 Mori, S., Leblond, C.P., 1969b. Identification of microglia in light and electron microscopy. J
790 Comp Neurol 135, 57-80.
791 Niwa, K., Araki, E., Morham, S.G., Ross, M.E., Iadecola, C., 2000. Cyclooxygenase-2
792 contributes to functional hyperemia in whisker-barrel cortex. J Neurosci 20, 763-770.
793 O'Doherty, D.C.M., Ryder, W., Paquola, C., Tickell, A., Chan, C., Hermens, D.F., Bennett,
794 M.R., Lagopoulos, J., 2018. White matter integrity alterations in post-traumatic stress
795 disorder. Hum Brain Mapp 39, 1327-1338.
796 Papadopoulos, M.C., Davies, D.C., Moss, R.F., Tighe, D., Bennett, E.D., 2000.
797 Pathophysiology of septic encephalopathy: a review. Crit Care Med 28, 3019-3024.
798 Pfister, D., Siegemund, M., Dell-Kuster, S., Smielewski, P., Ruegg, S., Strebel, S.P., Marsch,
799 S.C., Pargger, H., Steiner, L.A., 2008. Cerebral perfusion in sepsis-associated delirium.
800 Crit Care 12, R63.
801 Piazza, O., Cotena, S., De Robertis, E., Caranci, F., Tufano, R., 2009. Sepsis associated
802 encephalopathy studied by MRI and cerebral spinal fluid S100B measurement.
803 Neurochem Res 34, 1289-1292.
804 Pierrakos, C., Antoine, A., Velissaris, D., Michaux, I., Bulpa, P., Evrard, P., Ossemann, M.,
805 Dive, A., 2013. Transcranial doppler assessment of cerebral perfusion in critically ill

806 septic patients: a pilot study. Ann Intensive Care 3, 28.
807 Pierrakos, C., Attou, R., Decorte, L., Kolyviras, A., Malinverni, S., Gottignies, P., Devriendt,
808 J., De Bels, D., 2014. Transcranial Doppler to assess sepsis-associated encephalopathy
809 in critically ill patients. BMC Anesthesiol 14, 45.
810 Pollard, V., Prough, D.S., Deyo, D.J., Conroy, B., Uchida, T., Daye, A., Traber, L.D., Traber,
811 D.L., 1997. Cerebral blood flow during experimental endotoxemia in volunteers. Crit
812 Care Med 25, 1700-1706.
813 Rittirsch, D., Huber-Lang, M.S., Flierl, M.A., Ward, P.A., 2009. Immunodesign of
814 experimental sepsis by cecal ligation and puncture. Nat Protoc 4, 31-36.
815 Rosendahl, J., Brunkhorst, F.M., Jaenichen, D., Strauss, B., 2013. Physical and mental health
816 in patients and spouses after intensive care of severe sepsis: a dyadic perspective on
817 long-term sequelae testing the Actor-Partner Interdependence Model. Crit Care Med 41,
818 69-75.
819 Rosengarten, B., Hecht, M., Auch, D., Ghofrani, H.A., Schermuly, R.T., Grimminger, F.,
820 Kaps, M., 2007. Microcirculatory dysfunction in the brain precedes changes in evoked
821 potentials in endotoxin-induced sepsis syndrome in rats. Cerebrovasc Dis 23, 140-147.
822 Rosengarten, B., Hecht, M., Wolff, S., Kaps, M., 2008. Autoregulative function in the brain
823 in an endotoxic rat shock model. Inflamm Res 57, 542-546.
824 Schelling, G., Briegel, J., Roozendaal, B., Stoll, C., Rothenhausler, H.B., Kapfhammer, H.P.,
825 2001. The effect of stress doses of hydrocortisone during septic shock on posttraumatic
826 stress disorder in survivors. Biol Psychiatry 50, 978-985.
827 Schramm, P., Klein, K.U., Falkenberg, L., Berres, M., Closhen, D., Werhahn, K.J., David,
828 M., Werner, C., Engelhard, K., 2012. Impaired cerebrovascular autoregulation in
829 patients with severe sepsis and sepsis-associated delirium. Crit Care 16, R181.
830 Sharshar, T., Carlier, R., Bernard, F., Guidoux, C., Brouland, J.P., Nardi, O., de la

831 Grandmaison, G.L., Aboab, J., Gray, F., Menon, D., Annane, D., 2007. Brain lesions in
832 septic shock: a magnetic resonance imaging study. Intensive Care Med 33, 798-806.
833 Shen, Q., Huang, S., Duong, T.Q., 2016. T2*-weighted fMRI time-to-peak of oxygen
834 challenge in ischemic stroke. J Cereb Blood Flow Metab 36, 283-291.
835 Sicard, K., Shen, Q., Brevard, M.E., Sullivan, R., Ferris, C.F., King, J.A., Duong, T.Q., 2003.
836 Regional cerebral blood flow and BOLD responses in conscious and anesthetized rats
837 under basal and hypercapnic conditions: implications for functional MRI studies. J
838 Cereb Blood Flow Metab 23, 472-481.
839 Smith, S.M., Jenkinson, M., Johansen-Berg, H., Rueckert, D., Nichols, T.E., Mackay, C.E.,
840 Watkins, K.E., Ciccarelli, O., Cader, M.Z., Matthews, P.M., Behrens, T.E., 2006. Tract-
841 based spatial statistics: voxelwise analysis of multi-subject diffusion data. Neuroimage
842 31, 1487-1505.
843 Smith, S.M., Nichols, T.E., 2009. Threshold-free cluster enhancement: addressing problems
844 of smoothing, threshold dependence and localisation in cluster inference. Neuroimage
845 44, 83-98.
846 Smith, S.M., Padayachee, S., Modaresi, K.B., Smithies, M.N., Bihari, D.J., 1998. Cerebral
847 blood flow is proportional to cardiac index in patients with septic shock. J Crit Care 13,
848 104-109.
849 Soejima, Y., Fujii, Y., Ishikawa, T., Takeshita, H., Maekawa, T., 1990. Local cerebral
850 glucose utilization in septic rats. Crit Care Med 18, 423-427.
851 Stefanovic, B., Bosetti, F., Silva, A.C., 2006. Modulatory role of cyclooxygenase-2 in
852 cerebrovascular coupling. Neuroimage 32, 23-32.
853 Sun, D., Jakobs, T.C., 2012. Structural remodeling of astrocytes in the injured CNS.
854 Neuroscientist 18, 567-588.
855 Sun, D., Lye-Barthel, M., Masland, R.H., Jakobs, T.C., 2010. Structural remodeling of

856 fibrous astrocytes after axonal injury. J Neurosci 30, 14008-14019.
857 Swanson, L.W., 1998. Brain Maps: Structure of the Rat Brain. Elsevier, Amsterdam.
858 Tempel, G.E., Cook, J.A., Wise, W.C., Halushka, P.V., Corral, D., 1986. Improvement in
859 organ blood flow by inhibition of thromboxane synthetase during experimental
860 endotoxic shock in the rat. J Cardiovasc Pharmacol 8, 514-519.
861 Tsuruta, R., Oda, Y., 2016. A clinical perspective of sepsis-associated delirium. J Intensive
862 Care 4, 18.
863 Vachharajani, V., Cunningham, C., Yoza, B., Carson, J., Jr., Vachharajani, T.J., McCall, C.,
864 2012. Adiponectin-deficiency exaggerates sepsis-induced microvascular dysfunction in
865 the mouse brain. Obesity (Silver Spring) 20, 498-504.
866 Villega, F., Delpech, J.C., Griton, M., Andre, C., Franconi, J.M., Miraux, S., Konsman, J.P.,
867 2017. Circulating bacterial lipopolysaccharide-induced inflammation reduces flow in
868 brain-irrigating arteries independently from cerebrovascular prostaglandin production.
869 Neuroscience 346, 160-172.
870 Wichterman, K.A., Baue, A.E., Chaudry, I.H., 1980. Sepsis and septic shock--a review of
871 laboratory models and a proposal. J Surg Res 29, 189-201.
872 Williams, D.S., Detre, J.A., Leigh, J.S., Koretsky, A.P., 1992. Magnetic resonance imaging
873 of perfusion using spin inversion of arterial water. Proc Natl Acad Sci U S A 89, 212-
874 216.
875 Wintermann, G.B., Brunkhorst, F.M., Petrowski, K., Strauss, B., Oehmichen, F., Pohl, M.,
876 Rosendahl, J., 2015. Stress disorders following prolonged critical illness in survivors of
877 severe sepsis. Crit Care Med 43, 1213-1222.
878 Wyler, F., Forsyth, R.P., Nies, A.S., Neutze, J.M., Melmon, K.L., 1969. Endotoxin-induced
879 regional circulatory changes in the unanesthetized monkey. Circ Res 24, 777-786.
880 Wyler, F., Rutishauser, M., Weisser, K., 1972. Endotoxin induced regional circulatory

881 reactions in the rabbit with and without halothane anesthesia. J Surg Res 13, 13-19.
882 Yokoo, H., Chiba, S., Tomita, K., Takashina, M., Sagara, H., Yagisita, S., Takano, Y.,
883 Hattori, Y., 2012. Neurodegenerative evidence in mice brains with cecal ligation and
884 puncture-induced sepsis: preventive effect of the free radical scavenger edaravone. PLoS
885 One 7, e51539.
886 Yokota, H., Ogawa, S., Kurokawa, A., Yamamoto, Y., 2003. Regional cerebral blood flow in
887 delirium patients. Psychiatry Clin Neurosci 57, 337-339.
888 Young, G.B., 2013. Encephalopathy of infection and systemic inflammation. J Clin
889 Neurophysiol 30, 454-461.
890 Zrzavy, T., Hoftberger, R., Berger, T., Rauschka, H., Butovsky, O., Weiner, H., Lassmann,
891 H., 2019. Pro-inflammatory activation of microglia in the brain of patients with sepsis.
892 Neuropathol Appl Neurobiol 45, 278-290.

894 **Figure and table legend**s

895

896 *Figure 1*

897 Placement of different Region Of Interest 1: hemisphere; 2: corpus callosum; 3 external
898 capsule; 4 cortex and 5: striatum. (ROIs; A) used to analyze perfusion-weighted (example in
899 B), T2-weighted (example in C) and diffusion-weighted images (example in D).

900

901 *Figure 2*

902 Food intake relative to body weight (A) during 24h after CLP or sham surgery. Group size
903 Sham: n=9; CLP: n=11-12. Reflex scores: Pinna (B), corneal (C) and righting (D) reflexes at
904 24h, 12h, and 1h prior to surgery then 4h, 8h and 24h later. Group size Sham: n=8-9; CLP:
905 n=8-12.

906

907 *Figure 3*

908 Changes in T2-weighted intensity at the base of the brain (A), in the cortex (B), striatum (C)
909 and the corpus callosum (D). Graphs represent maximum intensities in the VOI relative to
910 that of the muscle 24h after laparotomy or cecal ligation and puncture. *: $p < 0.05$. Group
911 sizes Sham: n=8; CLP: n=11.

912

913 *Figure 4*

914 Perfusion distribution to rat cortex (A), striatum (B), corpus callosum (C) and external
915 capsule (D).Graphs represent perfusion relative to both hemispheres for all structures except
916 for the corpus callosum that was expressed relative to global brain 24h after surgery. *: $p <$
917 0.05; Group sizes Sham: n=8; CLP: n=12.

918

Figure 5

Changes in corpus callosum axial water diffusion at bregma -0.51mm (A) and left external capsule fractional anisotropy the at bregma -1.08mm (B) 24h after laparotomy or cecal ligation and puncture. *: $p < 0.05$. Group sizes Sham: n=7-8; CLP: n=12.

Figure 6

Photomicrographs illustrating the distribution of rat IgG-immunoreactivity in ventral hippocampal commissure (A,B), the corpus callosum (C,D), external capsule (E,F), dorsoslateral striatum (G,H) and hippocampus (I,J), 24 h after laparotomy (A, C, E, G, I) or cecal ligation and puncture (B, D, F, H, J) in rats. cc: corpus callosum; ec: external capsule; vhc: ventral hippocampal comissure; SFO: subfornical organ. Arrow heads > and < indicate perivascular diffuse cloud-like labeling Scale bar = 100µm.

Figure 7

Photomicrographs illustrating the distribution of COX-2-immunoreactivity in the ventromedial preoptic area (A, B), caudate putamen (C, D), external capsule (E, F), hippocampus (G, H) and cortex (I, J) 24h after laparotomy (A, C, E, G, I) or cecal ligation and puncture in rats (B, D, F, H, J). och: optic chiasm; ec: external capsule. Arrow heads > and < indicate labeling. Scale bar = 100 µm. Quantification of cortical COX-2-immunoreactive cells (K) and surface (L) 24h after cecal ligation and puncture or laparotomy. i.r.: immunoreactivity *: $p < 0.05$. Group sizes Sham: n=6; CLP: n=7.

Figure 8

Photomicrographs illustrating Iba1-ir microglia in the corpus callosum after laparotomy (A) or cecal ligation and puncture (B) in rats. Quantitative Fraclac-based analysis of microglial

944 height (C) and width (D) in the corpus callosum. i.r.: immunoreactivity *: $p < 0.05$. Group
945 sizes Sham: n=9; CLP: n=11. Scale bar = 100µm.
946
947 *Figure 9*
948 Photomicrographs illustrating GFAP-ir astrocytes in the corpus callosum after laparotomy
949 (A) or cecal ligation and puncture (B) in rats. Quantitative analysis of astrocyte height
950 (Fraclac; C) and the relative surface occupied by GFAP-ir fragments (D) in the corpus
951 callosum. i.r.: immunoreactivity ***: $p < 0.001$. Group sizes Sham: n=9; CLP: n=11. Scale
952 bar = 100µm.
953
954 *Figure 10*
955 Photomicrographs illustrating AQP4-ir astrocytes end-feet in the cortex after laparotomy (A)
956 or cecal ligation and puncture (B) in rats. Quantitative analysis of counts (C) and the relative
957 surface occupied (D) by AQP4-ir fragments in the cortex. i.r.: immunoreactivity ***: $p <$
958 0.001. Group sizes and the surface occupied by AQP-4. Sham: n=7; CLP: n=9. Scale bar =
959 50µm.
960
961 *Supplementary figure 1*
962 Location of differences in fractional anisotropy indicated by arrows as found in the left
963 striatum using Voxel-based analysis using tract-based spatial statistics (TBSS) with 5000
964 permutations in the horizontal (A), sagittal (B) and coronal plane (C).
965
966
967

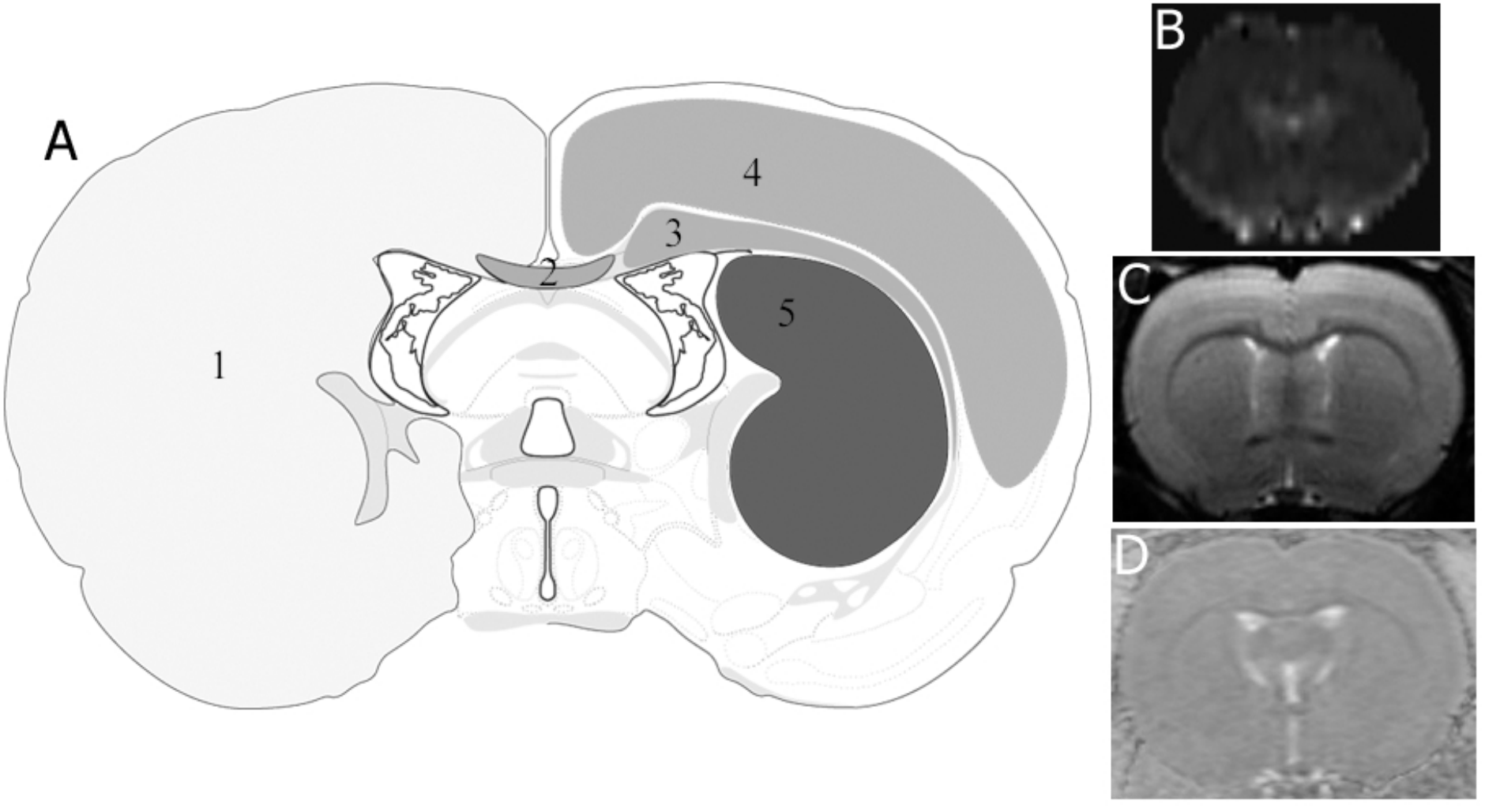
A
1
2
3
4
5
B
C
D

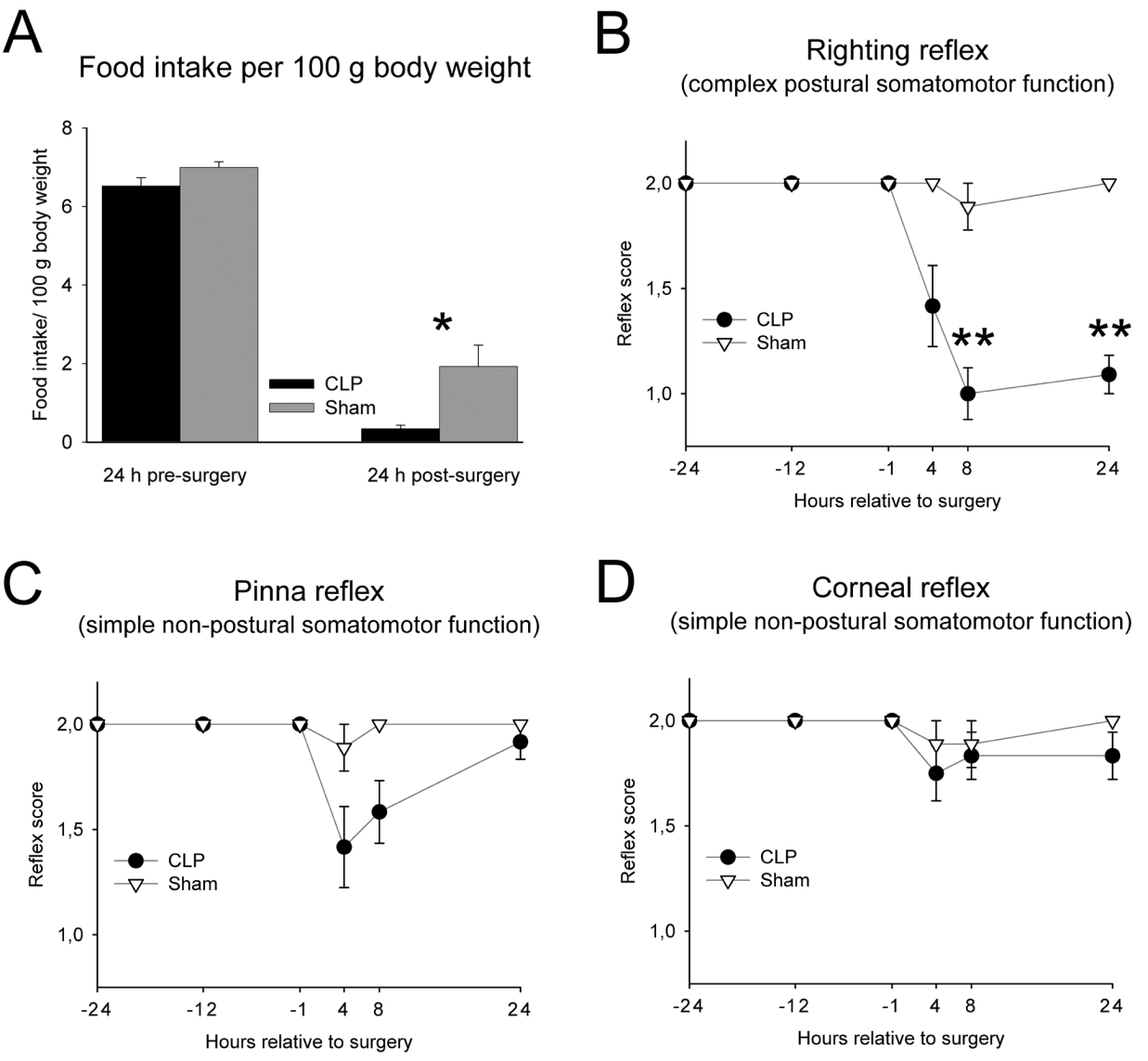

Fig. 2, Griton et al.

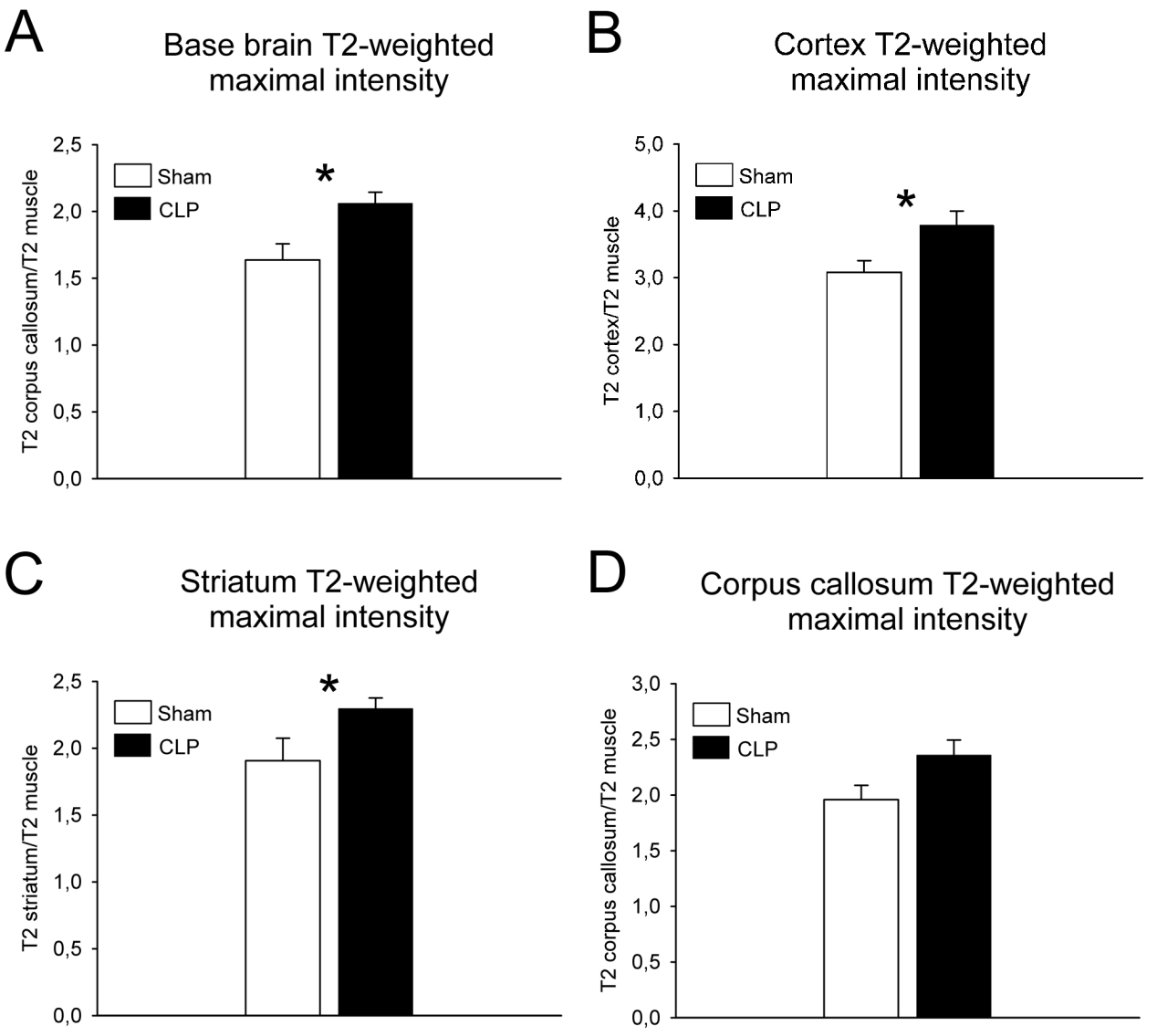

Fig. 3, Griton et al.

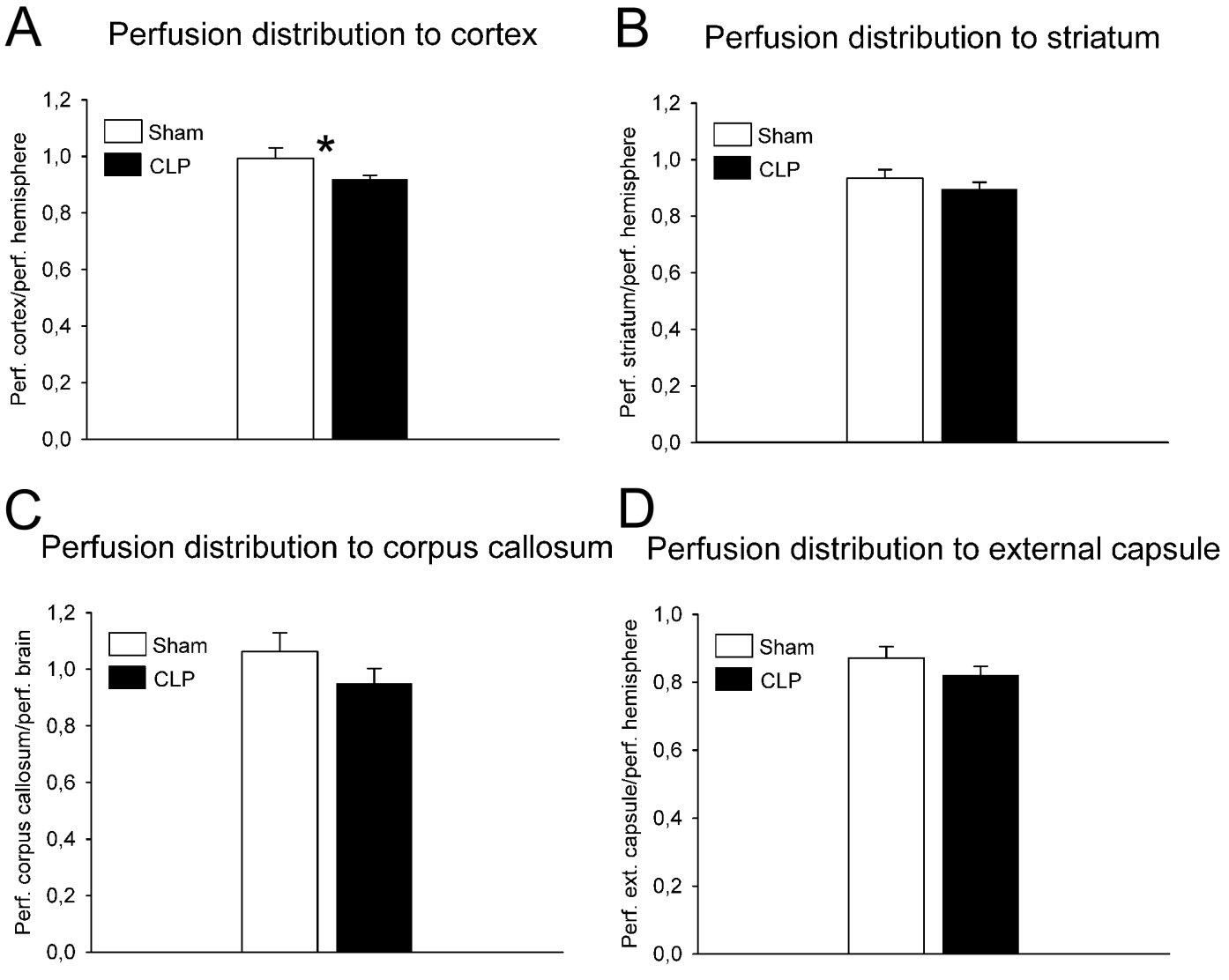

Fig. 4, Griton et al.

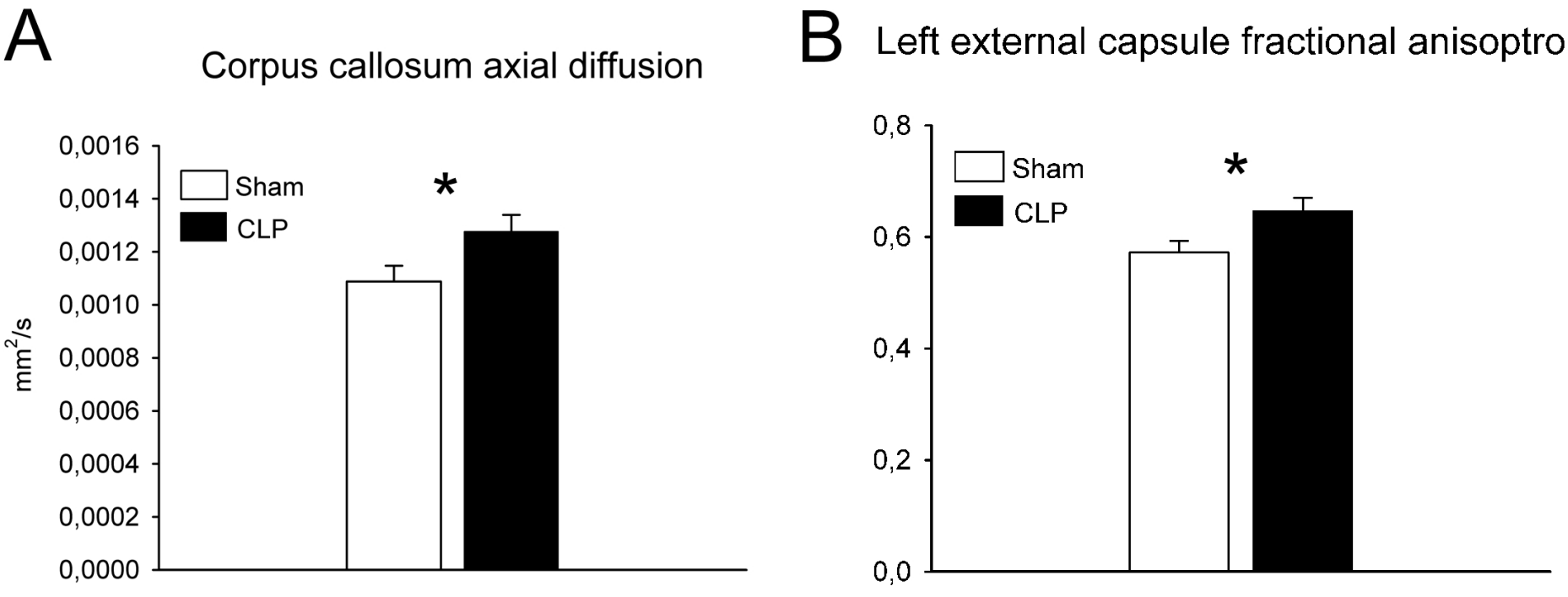

Fig. 5, Griton et al.

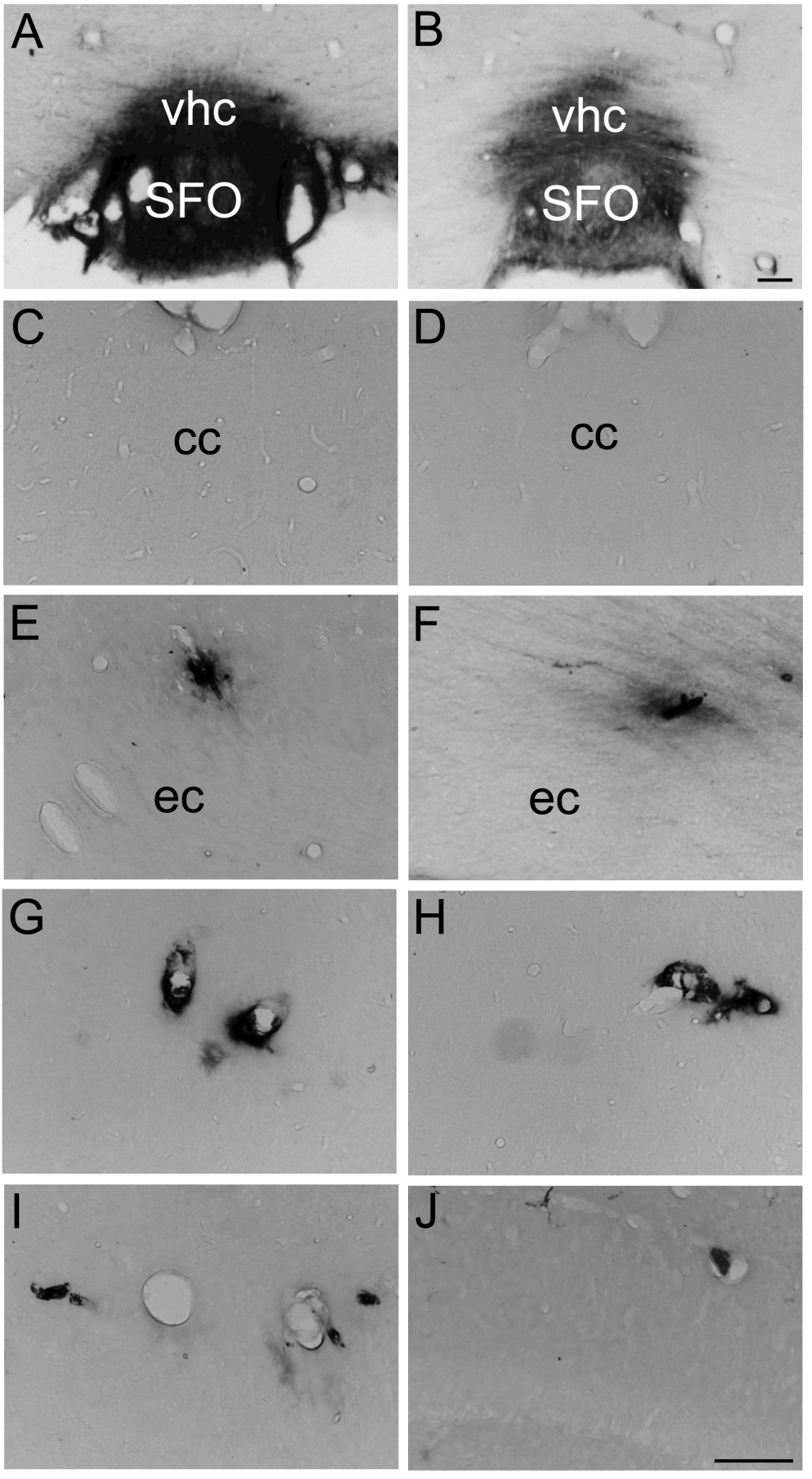

Griton et al., Fig. 6

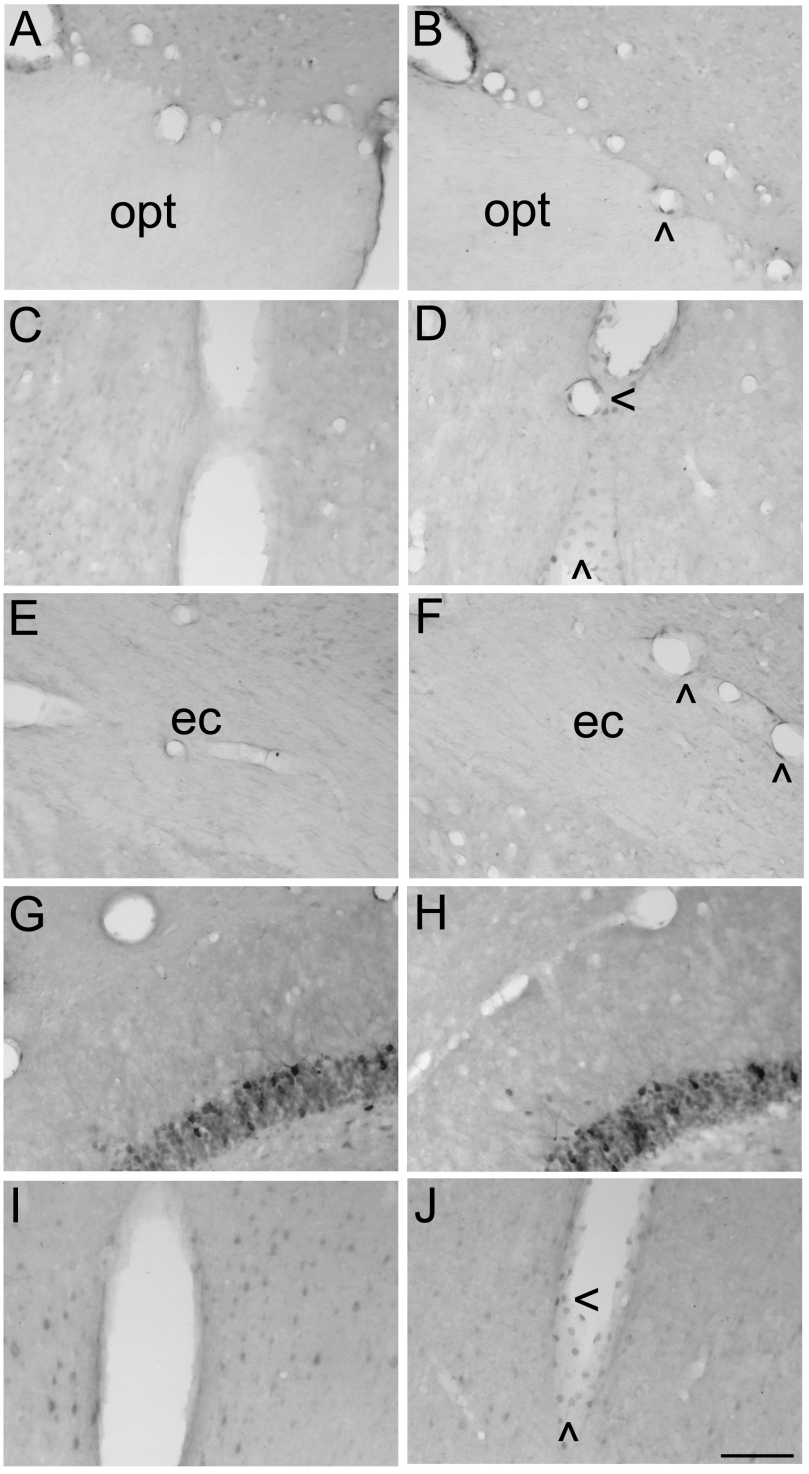

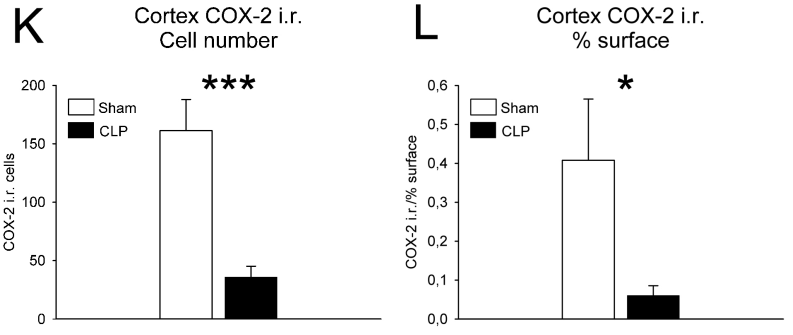

Griton et al., Fig. 7

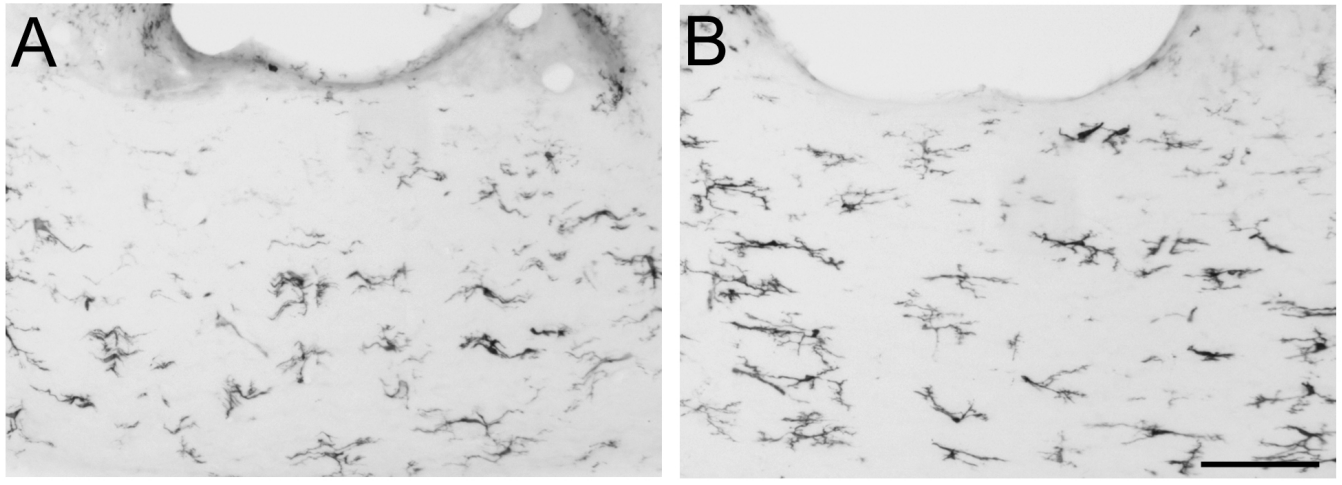

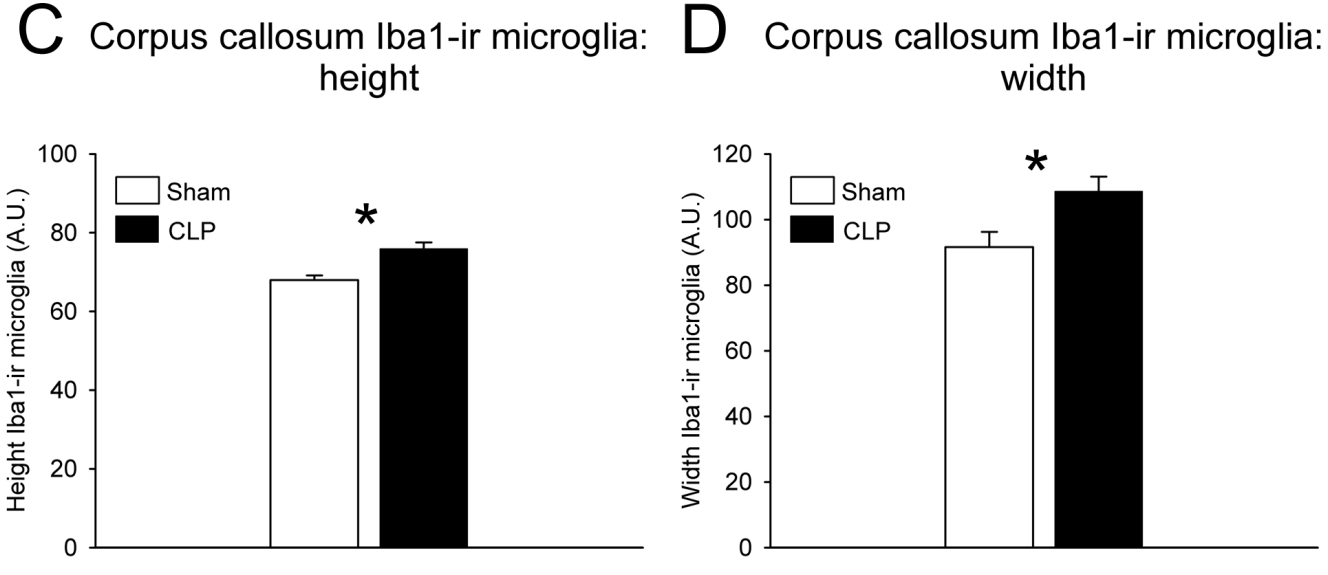

Griton et al., Fig. 8

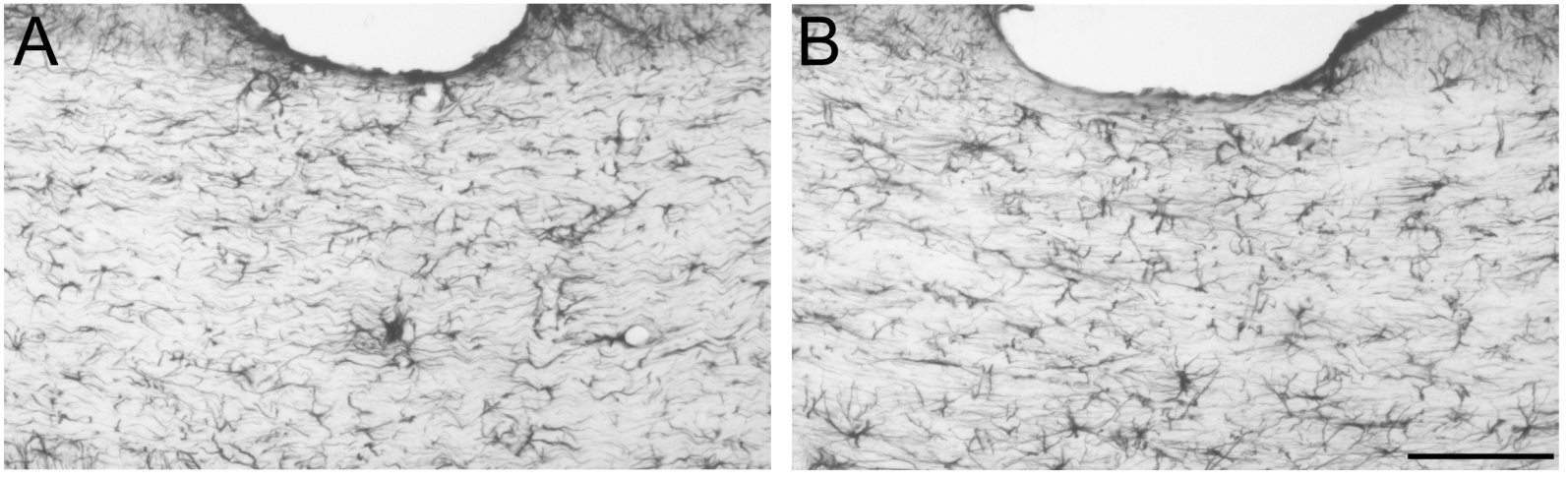

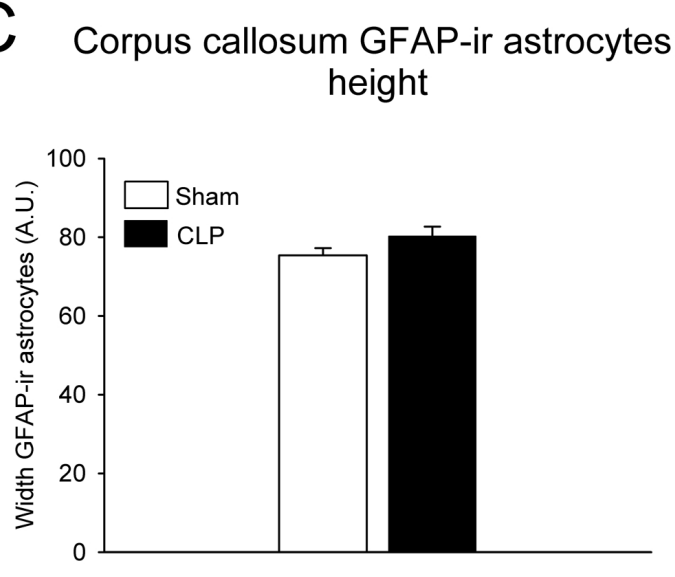

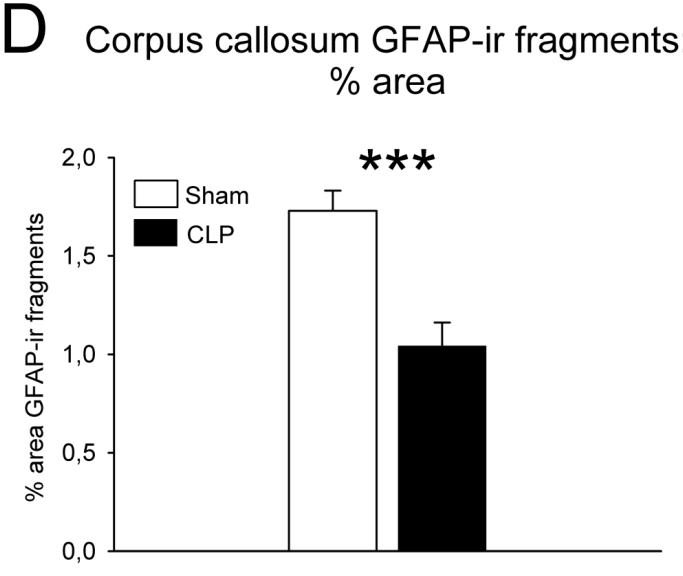

Griton et al., Fig. 9

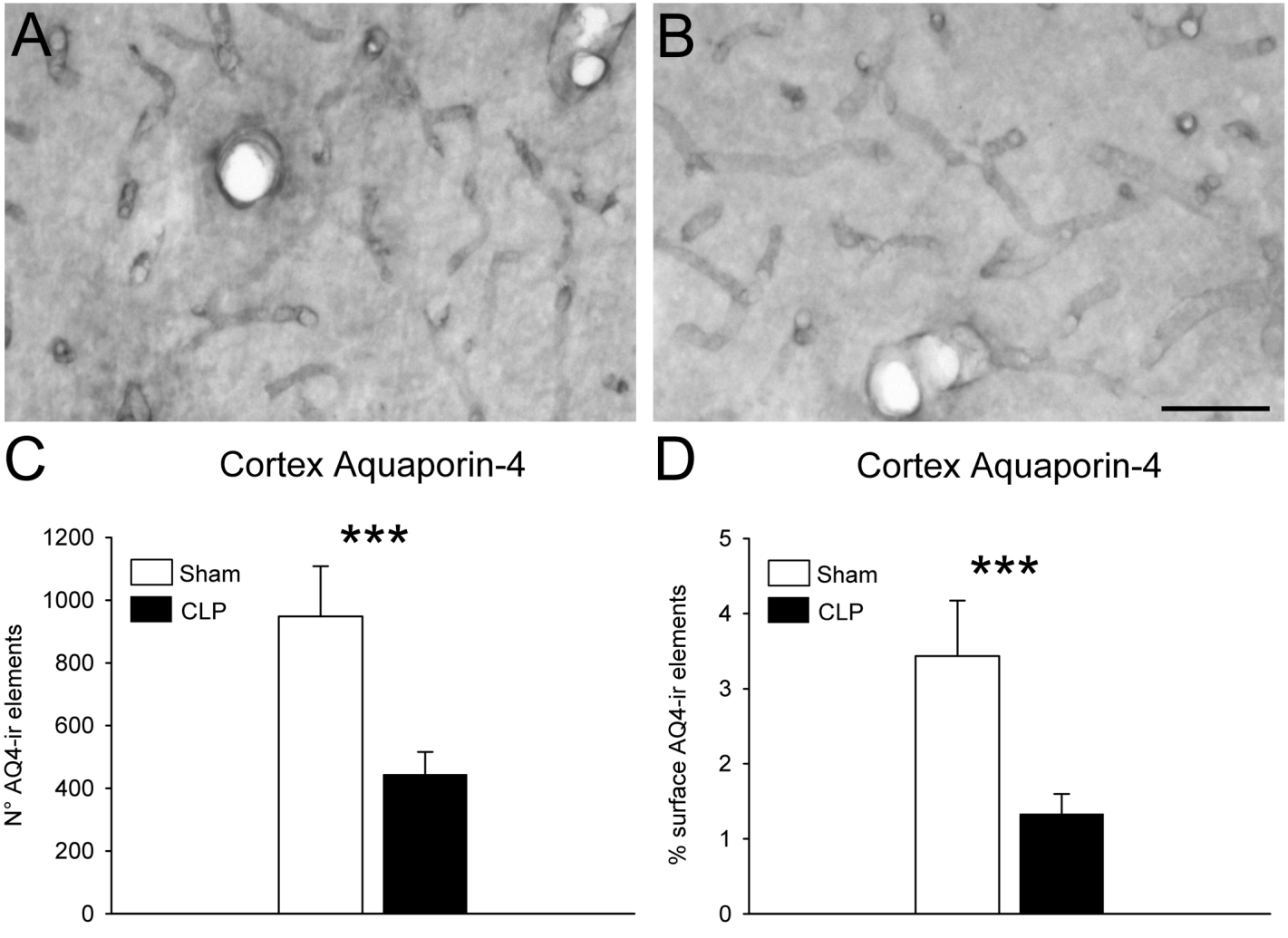

Griton et al., Fig. 10

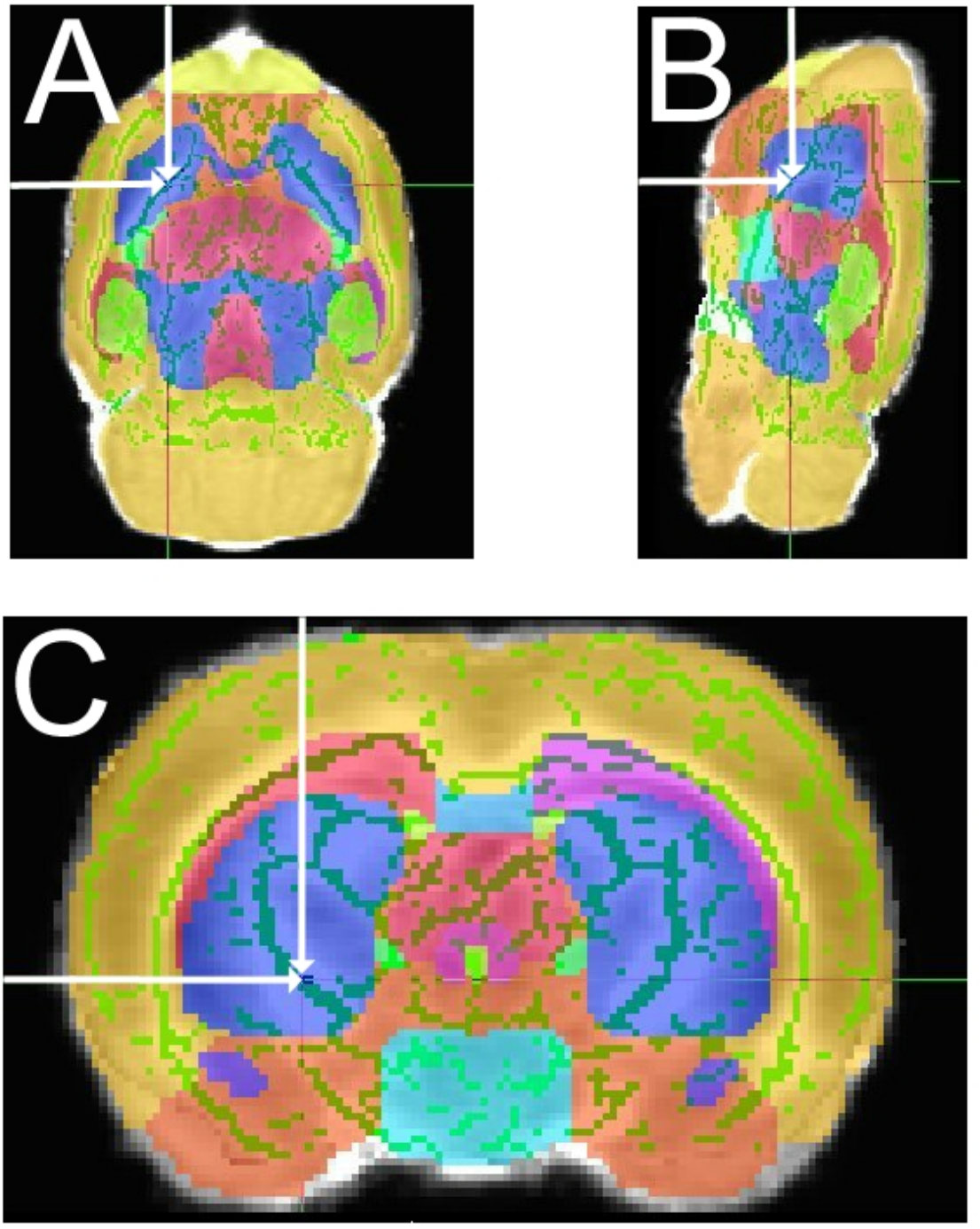

Griton et al.,
Suppl. Fig. 1

Supplementary figure 1

Location of differences in fractional anisotropy indicated by arrows as found in the left striatum using Voxel-based analysis using tract-based spatial statistics (TBSS) with 5000 permutations in the horizontal (A), saggital (B) and coronal plane (C).

Supplementary materials and methods

Magnetic Resonance Imaging

- T1-weighted MRI

T1-weighted images were obtained with a FLASH (Fast Low Angle Shot) pulse sequence with the following parameters: repetition time [TR]/echo time [TE]: 15/2.5ms; flip angle: 30°; voxel size: 117×117×234μm^3; Field of View (FOV): 30×30×30mm^3; acquisition time: 6 min.

- T2-weighted MRI

T2-weighted images were acquired using a Rapid Acquisition with Relaxation Enhancement (RARE) sequence with the following parameters: repetition time: 3.64s, echo time: 70ms, flip angle: 90°, RARE factor: 16, number adjacent (non-contiguous) axial slices: 20, slice thickness: 0.7mm, image matrix size: 196×196 pixels, FOV: 25×25mm^2 and in plan spatial resolution of 128μm, 8 averages were acquired giving a total acquisition time of 4min51s.

- Arterial Spin Labeling (ASL)

Arterial Spin Labeling data were acquired from a single 1.5 mm-thick axial slice, with a FOV of 35×35 mm^2 using a Flow-sensitive Alternating Inversion Recovery–Echo Planar Imaging) pulse sequence (FAIR-EPI) (Kim and Tsekos, 1997). The acquisition was performed twice, first with selective inversion of the slice and then with a global inversion recovery technique (Kober et al., 2004). For each of these acquisitions, and based on previous publications (Carr et al., 2007), the following parameters were used: TR/TE 16000/15ms; flip angle: 90°; number of averages: 6; inversion times: 0.2, 0.6, 0.8, 0.9, 1.0, 1.1, 1.2, 1.5, 2.0, and 2.5s; acquisition duration: 14min25s.

- Diffusion-weighted MRI (dMRI)

A Stejskal-Tanner Echo Planar Imaging (EPI) pulses sequence was used to collect diffusion-

weighted images (Stejskal and Tanner, 1965). A 3D multi-shot EPI dMRI pulse sequence was used to increase the sensitivity of diffusion- weighted MRI (Crombe et al., 2018; Tounekti et al., 2018). Twenty-one diffusion-weighted images were acquired with b-value =1000s/mm^2 applied along 21 non-collinear diffusion encoding directions (B1000 images) with a Stejskal-Tanner diffusion-sensitized acquisition scheme (Stejskal and Tanner, 1965). One other DW image was acquired with a b-value of 0s/mm2 (B0 image). DW-images were recorded with the following parameters: TR/TE=1200/36.86ms; voxel size: 153×148×333µm^3; FOV: 30×22×16mm^3; flip angle: 90°; acquisition duration: 22min4 s.

References

Crombe, A., Planche, V., Raffard, G., Bourel, J., Dubourdieu, N., Panatier, A., Fukutomi, H., Dousset, V., Oliet, S., Hiba, B., Tourdias, T., 2018. Deciphering the microstructure of hippocampal subfields with in vivo DTI and NODDI: Applications to experimental multiple sclerosis. Neuroimage 172, 357-368.

Kim, S.G., Tsekos, N.V., 1997. Perfusion imaging by a flow-sensitive alternating inversion recovery (FAIR) technique: application to functional brain imaging. Magn Reson Med 37, 425-435.

Stejskal, E.O., Tanner, J.E., 1965. Spin Diffusion Measurements: Spin Echoes in the Presence of a Time‐Dependent Field Gradient. J Chem Phys 42, 288.

Tounekti, S., Troalen, T., Bihan-Poudec, Y., Froesel, M., Lamberton, F., Ozenne, V., Clery, J., Richard, N., Descoteaux, M., Ben Hamed, S., Hiba, B., 2018. High-resolution 3D diffusion tensor MRI of anesthetized rhesus macaque brain at 3T. Neuroimage 181, 149-161.